Functionalized Silver Nanocubes for the Detection of Hazardous Analytes through SERS: Experimental and Computational Studies

Bhavya M. Basavaraja,[a] Ramya Prabhu Bantwal,[b] Anjana Tripathi,[c] Gautam Hegde,[d] Neena Susan John,[b] Ranjit Thapa,[c] Gopalkrishna Hegde,[d] R. Geetha Balakrishna,[a] Manav Saxena,[a] Ali Altaee,[e] Akshaya K. Samal[a]*

[a]Centre for Nano and Material Sciences, Jain University, Jain Global Campus, Ramanagara, Bangalore 562112, Karnataka, India

[b]Centre for Nano and Soft Matter Sciences, Jalahalli, Bangalore 560013, Karnataka, India

[c]Department of Physics, SRM University, Amaravati 522240, Andhra Pradesh, India

[d]Department of Instrumentation & Applied Physics, Indian Institute of Science, Bangalore-560012, Karnataka, India

[e]Centre for Green Technology, School of Civil and Environmental Engineering, University of Technology Sydney, 15 Broadway, Sydney 2007, New South Wales, Australia

Email: s.akshaya@jainuniversity.ac.in

Abstract

The functionalization of nanomaterials offers a significant impact on environmental protection. Three silver composites: silver nanocubes (Ag NCs) with cellulose (Ag-CE), Ag NCs with chitosan (Ag-CH), and Ag NCs with neutral alumina (Ag-NA) were synthesized with the incorporation of very low concentration of Ag NCs. The synthesized Ag-composites were used for the detection of hazardous analytes: 4-mercaptobenzoic acid (4-MBA), rhodamine 6G (R6G), and methylene blue (MB) via a highly sensitive surface-enhanced Raman scattering (SERS) technique. The enhancement factor (EF) for the detection of MB was found to be 1.2×10^6, 1.4×10^6, and 3.7×10^5 using Ag-CE, Ag-CH, and Ag-NA, respectively. A limit of detection (LOD) of 1 nM, 100 pM, and 100 μM was achieved for MB using Ag-CE, Ag-CH, and Ag-NA, respectively. The Ag-CH composite achieved excellent sensitivity and enhancement for the detection of MB compared to the other two Ag-composites. The order of detection efficiency of MB using Ag-composites was measured theoretically and follows the order, Ag-CH > Ag-CE > Ag-NA. A real-time filtration unit showed excellent efficiency for MB removal. The present method can be employed in commercial filtration processes for the benefit of the environment and sustainable development.

Keywords: Silver nanocubes (Ag NCs); Cellulose (CE); Chitosan (CH); Neutral alumina (NA); Methylene blue (MB); Filtration

Introduction

Functionalized nanoparticles have proliferated as promising solutions for environmental problems within the diverse variety of nanomaterials. Implementation of bare nanomaterials has a few challenges or limitations, such as instability, agglomeration, and reusability.[1] Functionalization of nanomaterials provides an excellent advantage on cost-effectiveness and enriches the properties in several folds.[2] Functionalization of the nanomaterial's surface offers the opportunity to tune their properties to overcome the current limitations of bare nanomaterials and improve the activity, stability, and selectivity of the materials.[3] The use of composites is one of the better solution for cost-effectiveness and large-scale use of materials in industrial applications.[4] Environmental contamination occurs in different ways, such as the use of dyes, pesticides, heavy metal ions, the release of toxic gases, and other organic pollutants into the environment without proper pre-treatment.[5-8] Environmental contamination causes pollution of air, water, and soil to a large extent and impact detrimental effects in humans and other living entities.[6,7] Industries are the main source of dye-based water contamination where the dye-contaminated water is released to water bodies without proper pretreatment. As a result, the fresh water sources get contaminated and a threat to humans as well as aquatic life. The wastewater from textile industries is the most polluted of all the industrial sectors with regard to the volume of waste generated and the composition of the effluent.[9] Furthermore, the rise in demand for textile objects and corresponding increase in manufacturing, as well as the use of synthetic dyes, has become one of the most significant sources of serious pollution concerns in recent times.[10] General techniques used to purify dye contaminated water include adsorption method, membrane technology, electrochemical process, advanced oxidation method, microbial technology, and photocatalytic degradation.[11] The adsorption method provides a number of advantages over other approaches, including a simple design and the potential for high performance at a low cost. Adsorption is a technique that is commonly used to remove organic and inorganic contaminants from industrial wastewater, and it has drawn a lot of interest for many researchers.[12]

4-mercaptobenzoic acid (4-MBA) is an organic pollutant[13] and rhodamine 6G (R6G) is a cationic dye, affect human health and pose a threat to the environment.[14] R6G is hazardous to nature and humans because of its chronic toxicity, carcinogenicity, reproductive, and developmental toxicity. Methylene blue (MB) is a cationic dye that affects the esophagus and stomach. It causes nausea, vomiting, diarrhea, dizziness, headache, fever, anemia, discoloration of urine, bladder irritation, etc.[15] Because of these hazardous effects, detection of harmful contaminants is highly essential to protect the human and environment. Surface-enhanced Raman scattering (SERS) is one of the premium tools for the detection of these contaminants, due to its convenient sample preparation, and high sensitivity towards detection of contaminants.[6] Hence, in this work, SERS technique is implemented to detect the contaminants using Ag-composites. In the synthesis of composites, the selection of support materials needs to be taken care of. Support material should be economical, non-toxic, and environmentally friendly. Among different support materials, cellulose (CE), chitosan (CH), and neutral alumina (NA) were opted because of their excellent characteristics and eco-friendly nature.[16-18]

Many research groups have synthesized composites for the detection of MB. Chettri and coworkers synthesized composite with RGO as a support material and reported a loading of 10 M Ag NPs.[19] Ag NPs-RGO composite was used for the detection of MB and achieved a limit of detection (LOD) of 10^{-8} M.[19] Multi-walled carbon nanotubes (MWCNTs) composite was synthesized by loading of10×10^{-3} M Ag NPs (MWCNTs-Ag) and detected MB at 10^{-7}M.[20] Fe_3O_4/GO/Ag was used as a composite with 14.7×10^{-3} M Ag NPs loading and detected MB at 10^{-9} M.[21] Lee and Chin fabricated a SERS substrate by the deposition of Ag NCs over polydimethylsiloxane (PDMS). 1.31×10^{-3} M concentration of Ag NCs was used for the substrate fabrication and detected MB as low as 10^{-9} M.[22] Ag coated magnetic polymethacrylate core-shell NPs were used as the substrate for the detection of MB at 10^{-7} M with 70.6×10^{-6} M Ag loading.[23] The details of composites, concentration of Ag loading, and LOD of MB reported in the literature and present work are compared and tabulated in Table 1 in the results and discussion. There are other substrates synthesized for SERS application with higher loadings of nanostructures were observed.[22,24,25] From the literature, it is observed that loading of high concentration of nanomaterials onto support materials results in enhanced performance. The use of high concentration nanomaterials is not

economical. Hence, keeping this factor in mind, the present work synthesized composites with very low concentration loading of Ag NCs for contaminants detection via SERS.

In the present work, three support materials: CE, CH, and NA were used to synthesize three Ag-composites, namely, Ag NCs with cellulose (Ag-CE), Ag NCs with chitosan (Ag-CH), and Ag NCs with neutral alumina (Ag-NA). Herein, low concentration of 0.2 wt % Ag NCs were added to all three support materials, individually, to synthesize three Ag-composites. These composites were used for the detection of 4-MBA, R6G, and MB via Raman analysis. SERS has been performed only for MB dye with three Ag-composites because of its high sensitivity compared to other contaminants. Among the three Ag-composites, Ag-CH provided excellent enhancement for MB and lower LOD compared to the other two composites. The enhancement factor (EF) for Ag-CE, Ag-CH, and Ag-NA towards MB detection was found to be 1.2×10^6, 1.4×10^6, and 3.7×10^5, respectively. A LOD of 1 nM, 100 pM, and 100 μM was achieved for Ag-CE, Ag-CH, and Ag-NA, respectively, for MB detection. All the samples exhibited good uniformity and a relative standard deviation (RSD) of 9.7, 8.6, and 12.9% were achieved for MB detection with Ag-CE, Ag-CH, and Ag-NA, respectively. A control experiment was carried out to determine the individual effects of Ag NCs and bare support materials for MB detection. This study confirmed that the low concentration of MB was detected due to the strong sustenance of support materials for Ag NCs to adsorb on them and the formation of Ag-S bond directly between Ag NCs and MB. Hence, the composite materials with low concentration loading of Ag NCs is the better option for sensing and also in terms of cost-effectiveness and environmental safety. The density functional theory (DFT) was performed, and the order of detection efficiency of MB follows Ag-CH > Ag-CE > Ag-NA with respect to the binding energy. The calculated adsorption energies for MB with Ag-CE, Ag-CH, and Ag-NA molecules are -5.57 eV, -5.98 eV, and -5.30 eV, respectively. This shows that Ag-CH has more capacity for MB adsorption. Hence, the result from the theoretical study is well matched with the experimental result.3D finite-difference time-domain (FDTD) was implemented for three different geometrical configurations of single, dimer and trimer Ag NCs and EF found to be 1.4×10^2, 8×10^6, and 6×10^6, respectively. A real-time filtration unit was made to filter MB using all three Ag-composites. Ag-CE and Ag-CH composites showed better adsorption of MB compared to Ag-NA. The filtration process is fast and effective. The composites used in the present

work can detect two or more contaminants, especially MB at a lower concentration, even with low concentration loading of Ag NCs and this work can be extended in large-scale filtration processes.

Materials and methods

The detailed materials and methods are given in SI.

Experimental Section

Synthesis of Ag NCs

The one-pot method was employed for the synthesis of Ag NCs as reported elsewhere[6,26] and detailed protocol is mentioned in supporting information (SI).

Synthesis of Ag-composites

For the synthesis of Ag-composites, 2 g of CE, CH, and NA were taken individually in a 20 mL glass vial and 10 mL of 0.2 wt% (0.18 nM) purified Ag NCs was added and stirred for 1 h. After 1 h, the color of the support materials turns slightly yellow due to the adsorption of Ag NCs. Later the composite solutions were transformed into petri dish and dried at 100 °C for 4 h. Ag NCs with CE, CH, and NA were labeled as Ag-CE, Ag-CH, and Ag-NA, respectively.

SERS substrate preparation

5 mg of each of the three Ag-composites were taken in an eppendorf tube and 1 mL of MB at various concentrations (ranging from 10^{-5} to 10^{-11} M) was added. Further, the mixture was thoroughly mixed under a vertex mixer for 1 minute to attain proper interaction between Ag-composites and MB. The eppendorf tube was then left for approximately 5 minutes to allow the suspension of MB adsorbed Ag-composites (Ag-composites-MB) to settle. The unreacted MB in the supernatant was thereafter pipetted out and discarded. The leftover (Ag-composites-MB) slurry was transferred onto a glass slide, allowed to dry in ambient conditions, and then subjected to SERS analysis. The same procedure is followed to prepare all the SERS samples.

Results and discussion

UV-vis analysis was performed for synthesized Ag NCs and shown in Fig. 1A. Ag NCs exhibits three peaks in UV-vis spectra corresponding to different localized surface plasmon resonance

mode. The main surface plasmon resonance peak observed at 457 nm, ascribed to excitation of dipolar charge distribution. Two shoulder peaks observed at 399 and 353 nm assigned to quadrupolar and octupolar mode, respectively. All the peaks of Ag NCs were assigned and are well matched with literature.[22,27] FESEM analysis reveals the nanocube morphology of the nanostructure, shown in Fig. 1B. FESEM image of Ag NCs shows that the NCs are nearly monodispersed in nature. Side and diagonal length of Ag NCs found to be 43 ± 2 and 58 ± 2 nm, respectively.

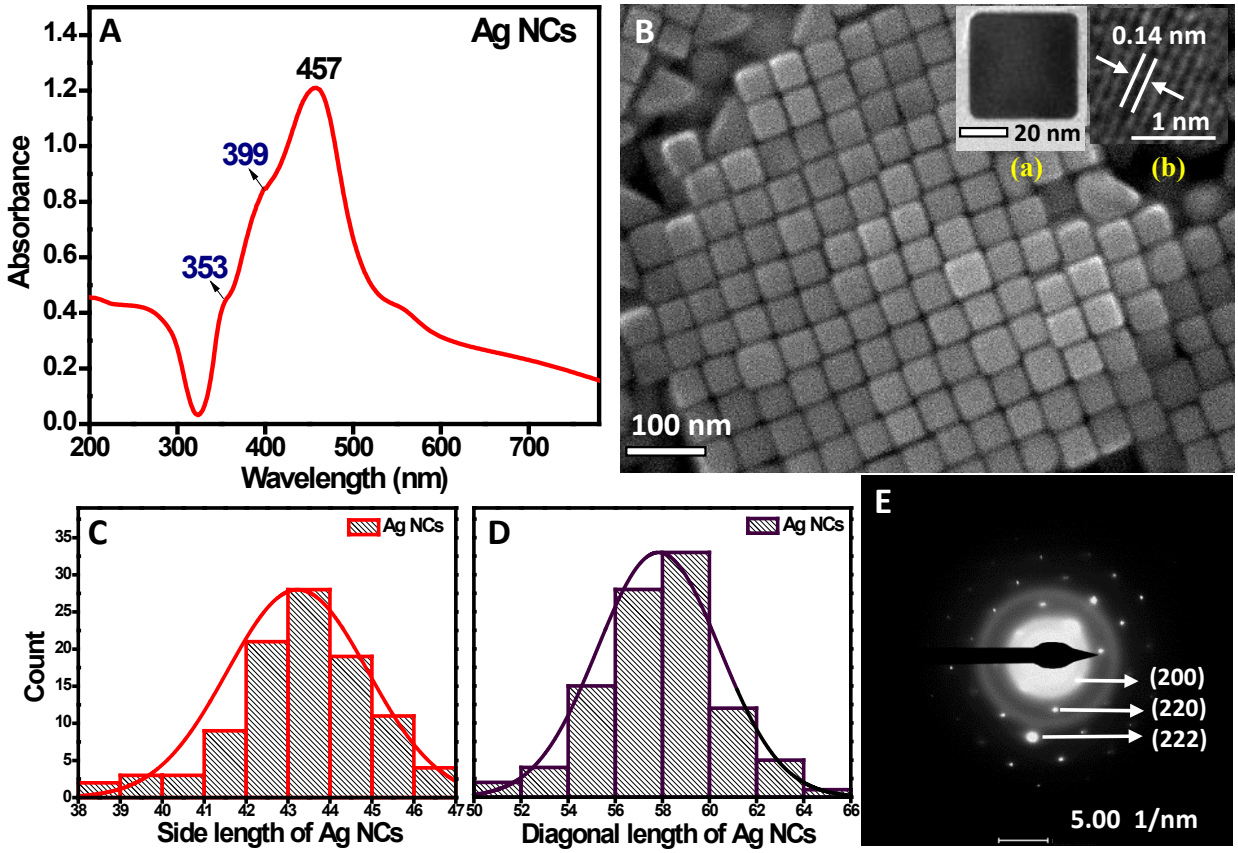

Figure 1. (A) UV-vis spectrum, (B) FESEM image of Ag NCs, (C and D) histogram of the size distribution of Ag NCs along the side and diagonal length, respectively, and (E) SAED pattern of Ag NCs. The inset of (B) display the (a) TEM image of Ag NC and (b) shows the interplanar distance of Ag lattice.

The inset of Fig. 1B shows the TEM image of Ag NC (Fig. 1B (a)) which is comparable with the side and diagonal length obtained from the FESEM analysis. Crystalline nature was confirmed by HRTEM analysis, provided with the d-spacing value of 0.14 nm corresponds to (220) plane of Ag

as shown in Fig. 1B (b). Histogram was plotted for the side and diagonal length of Ag NCs, displayed in Fig. 1C and D, respectively. SAED pattern shown in Fig. 1E shows different interplanar distances match with different planes of Ag. The obtained interplanar distances of 0.20, 0.14, and 0.11 nm are correspond to the planes of (200), (220), and (222), respectively.

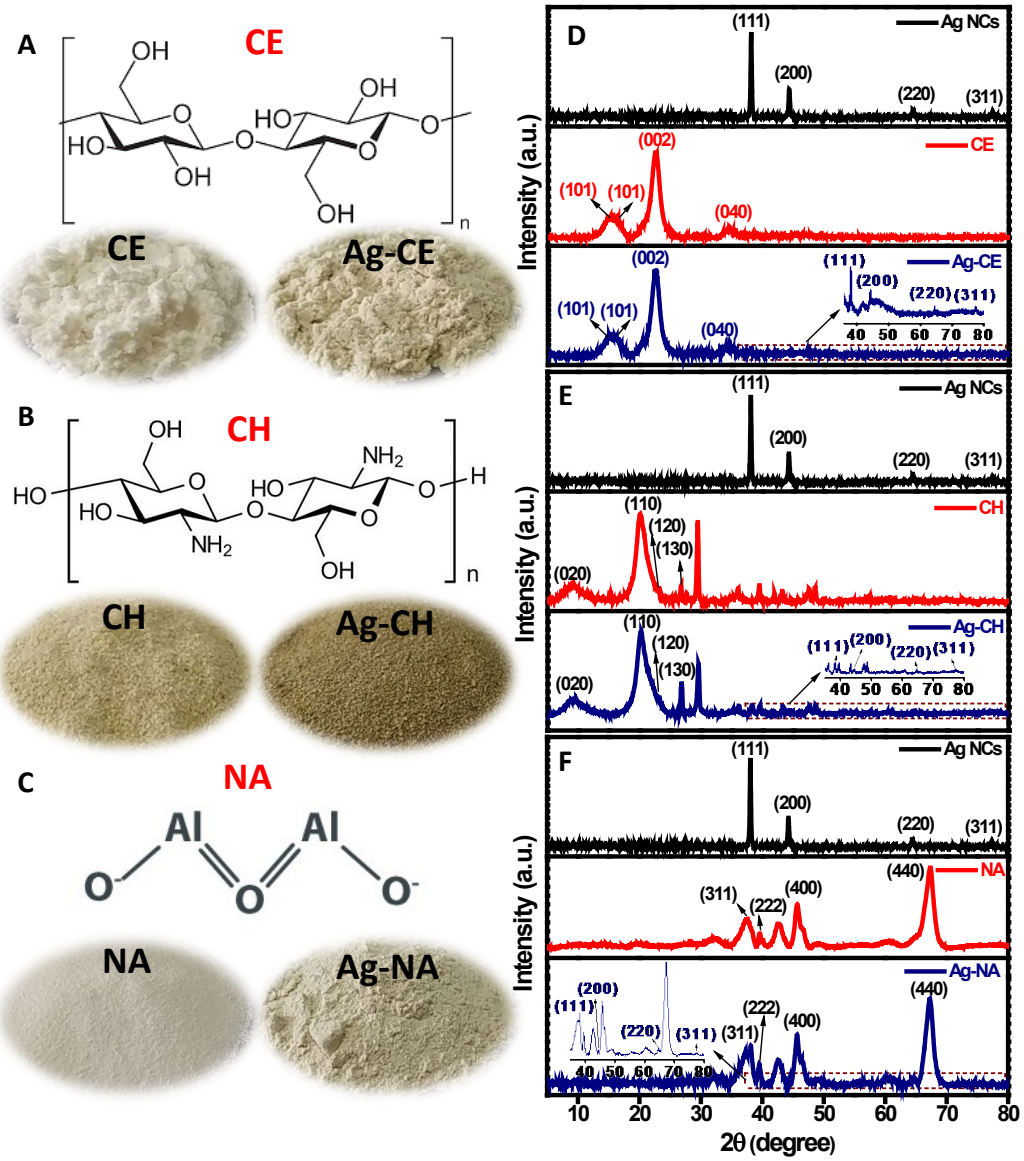

Figure 2. Structure and image of (A) CE, Ag-CE, (B) CH, Ag-CH, and (C) NA, Ag-NA. (D), (E), and (F) displays PXRD analysis of CE, CH, and NA, respectively, along with their Ag-composites.

The structure of CE, CH, and NA are shown in Fig. 2A, B, and C, respectively. Photographic images of CE, CH, and NA before and after interaction with Ag NCs i.e., Ag-CE, Ag-CH, and Ag-NA are shown in Fig. 2A, B, and C, respectively. It is clearly observed that color of CE, CH, and

NA changed after adsorption of Ag NCs. All the Ag-composites were subjected to PXRD analysis to confirm the crystalline nature and phases of materials. Fig. 2D, E, and F displayed PXRD spectra of all Ag-composites. XRD spectrum of Ag-composites is compared with Ag NCs and respective support material. Ag NCs displayed four major peaks of 2θ values at 38.0, 44.2, 64.3, and 77.3 corresponding to h, k, l values (111), (200), (220), and (311), respectively. All the peaks are indexed to fcc silver and well-matched with the literature (JCPDS file no. 04-0783).[28] XRD spectra of CE and Ag-CE is shown in Fig. 2D. CE shows 2θ values at 15.0, 16.1, 22.5, and 34.5 corresponds to (101), (101), (002) and (040), respectively.[29] XRD spectra of Ag-CE shows all the planes of CE along with Ag, where 2θ values at 38.1, 44.3, 64.3, and 77.4 which corresponds to (111), (200), (220), and (311) planes of Ag and these planes are present in all the composites. As the loading of Ag NCs is very low in concentration (0.2 wt%), peak intensities are low for Ag NCs and hence, magnified planes of Ag in all the composites are shown as an inset in Fig. 2D, E, and F. Fig. 2E shows the XRD pattern of CH and Ag-CH, where 2θ values at 9.1, 20.1, 23.0, and 26.7 corresponds to (020), (110), (120), and (130), respectively. Ag-CH contains all planes of CH along with Ag planes.[30] NA and Ag-NA XRD patterns are shown in Fig. 2F, where 2θ values at 38.1, 39.4, 45.7, and 67.2 are corresponds to (311), (222), (400), and (440) planes. Ag-NA contains all planes of NA and Ag NCs.[31] It is clearly evident that all the Ag-composites contains planes of Ag NCs as well as the planes of respective support materials. Hence, XRD analysis confirms that Ag NCs are adsorbed on CE, CH, and NA.

FESEM analysis was performed for the Ag-composites, which confirms the adsorption of Ag NCs on the CE, CH, and NA support materials. As the loading of Ag NCs is very much lower, only a few NCs can be seen and the main motto is to get better SERS activity with low concentration loading of Ag NCs. Fig. S1 shows the FESEM image of all the Ag-composites. FESEM images of Ag-CE are displayed in Fig. S1 (A and D), which shows the adsorption of Ag NCs on CE. The inset in Fig. S1D is the high-resolution FESEM image of Ag-CE. Fig. S1 (B and E) are the FESEM images of Ag-CH, and the inset in Fig. S1E is the high-resolution FESEM of Ag-CH. NA is a porous material, and hence, the Ag NCs were slightly embedded inside the alumina matrix. The FESEM images of Ag-NA are shown in Fig. S1 (C and F). A high-resolution image of Ag-NA is shown as an inset in Fig. S1F. Three Ag-composites were measured for TEM analysis to further

confirm the morphology and distribution of Ag NCs over support materials. Fig. 3A, B, and C show the large area TEM of Ag-CE, Ag-CH, and Ag-NA, respectively.

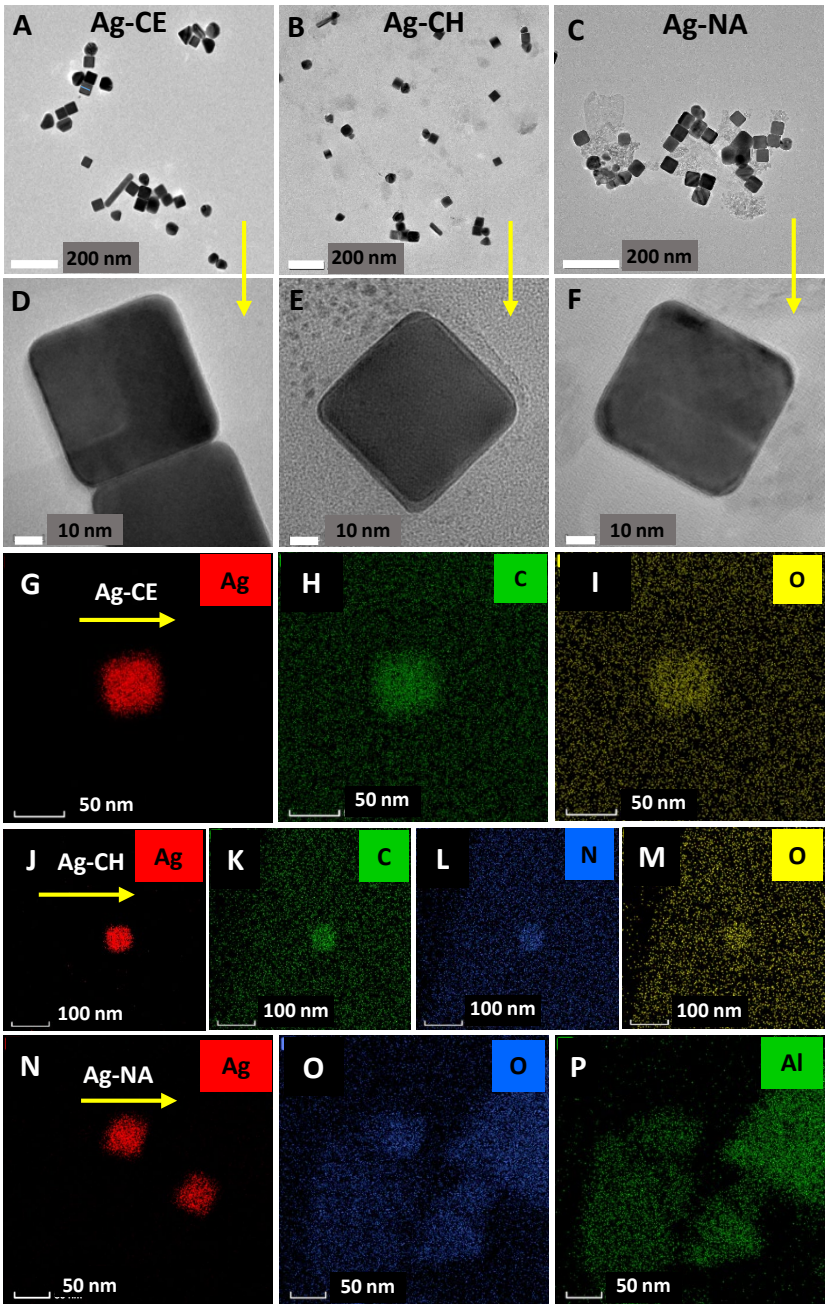

Figure 3. TEM image of (A) Ag-CE, (B) Ag-CH, and (C) Ag-NA. (D), (E), and (F) are the HRTEM images of Ag-CE, Ag-CH, and Ag-NA, respectively. Elemental mapping of (G-I) Ag-CE, (J-M) Ag-CH, and (N-P) Ag-NA.

Large area TEM shows the distribution of Ag NCs over support materials CE, CH, and NA, further confirms the NC morphology. Fig. 3D, E, and F shows the HRTEM image of Ag-CE, Ag-CH, and Ag-NA. Fig. S1G, H, and I display the TEM images of Ag-CE, Ag-CH, and Ag-NA, respectively, with marking in different colors. The blue, green, and orange markings represent the single, dimer, and trimer present after interaction with different supports with Ag NCs, respectively. Elemental mapping analysis has been performed to know the presence of Ag NCs in the support material. Fig. 3 represents the elemental mapping of all the Ag-composites. Fig. 3G-I represents the elemental mapping of Ag-CE, where Fig. 3G, H, and I represent Ag (red), C (green), and O (yellow), respectively. Fig. 3J-M represents the elemental mapping of Ag-CH and Ag (red), C (green), N (blue), and O (yellow) are represented in Fig. 3J, K, L, and M, respectively. Elemental mapping of Ag-NA shown in Fig. 3N-P. Here, Ag (red), O (blue), and Al (green) are represented in Fig. 3N, O, and P, respectively.

Cumulative mapping and line scan profile of all the elements present in the composite are shown in Fig. S2. Ag, C, and O are the main elements present in Ag-CE composite and their cumulative elemental mapping shown in Fig. S2A. Ag-CH is composed of Ag, C, N, and O as main elements and are simultaneously shown in Fig. S2C. Ag, Al, and O are the main elements present in Ag-NA composite and cumulatively shown in Fig. S2E. Elemental mapping shows that the elements of support material and Ag are present in all Ag-composites. Hence, elemental mapping confirms the adsorption of Ag NCs over support materials in the composites. The line scan profile was carried out for all the Ag-composites, shows the analysis of a selected line on the cumulative mapping image. The line scan shows the position (in nm) along the x-axis and integrated counts along the y-axis. Fig. S2B is the line scan profile along the line in Fig. S2A and provides information about the distribution of Ag, C, and O elements of Ag-CE. Fig. S2D is the line scan of Ag-CH and shows the distribution of Ag, C, N, and O. Fig. S2F displays the line scan profile of Ag-NA composite which gives the information of the distribution of Ag, Al, and O elements. Line scan analysis is strongly evident forthe adsorption of Ag NCs over CE, CH, and NA.Energy-dispersive X-ray spectroscopy (EDS) analysis was performed, which further provides evidence for the adsorption of Ag NCs over support materials in the Ag-composites. Fig. S3A, B, and C display the TEM-EDS spectrum of Ag-CE, Ag-CH, and Ag-NA, respectively. Fig. S3A shows the presence of Ag, C, and O elements of Ag-CE. Fig. S3B shows EDS spectrum of Ag-CH, which composes of Ag,

C, N, and O elements.Fig. S3C is the EDS spectrum of Ag-NA which represents Ag, Al, and O elements.

FT-IR analysis was performed to understand the adsorption of Ag NCs over support materials in the Ag-composites. FT-IR analysis of Ag NCs, support materials, and Ag-composites were shown in Fig. S4. Ag NCs are stabilized by cetyltrimethylammonium chloride (CTAC), hence, the bands at 2925 and 2854 cm^{-1} are assigned to symmetric and asymmetric stretching of -CH_2- of CTAC chain, respectively.[32] FT-IR spectrum of CE shows a band at 3432 cm^{-1} corresponds to a hydroxyl group (-OH) stretching, 2900 and 1374 cm^{-1}bandsare assigned to stretching and deformation vibrations of C-H groups in glucose unit.[33] The peak at 899 cm^{-1} is the characteristic peak of β-glycosidic linkage between glucose units, 1453 cm^{-1}band is attributed to tensile vibrations of C-O group. 1008 cm^{-1} peak represents (–C–O–C) pyranose ring skeletal vibration in CE.[33] FT-IR spectra of CH shows a strong band at 3523 cm^{-1} labeled for OH stretching vibration.[34] Bands at 2925 and 2854 cm^{-1} are allotted for symmetric and asymmetric stretching of C-H group, respectively. The 1546 and 1610 cm^{-1} bands represents N-H bending of amide II and N-H bending of primary amine, respectively in CH. The CH_2 bending and CH_3 symmetrical deformations were confirmed by the presence of bands at 1422 and 1375 cm^{-1}, respectively.[34] The band at 1153 cm^{-1} is assigned to asymmetric stretching of C-O-C bridge. Band at 1673 cm^{-1} corresponds to CO-NH_2 group in CH. 947 and 877 cm^{-1} bands are assigned to amine group of CH.[35] The band at 1546 cm^{-1}, slightly increased in Ag-CH because of the interaction between Ag NCs and amine group of CH. NA displayed a band at 3490 cm^{-1} corresponds to OH stretching.[36] Band at 1623 cm^{-1} is allotted to H-O-H vibrations and mainly a small band at 1046 cm^{-1} is assigned for Al-O-H vibration.[37] All the vibrations in the support materials are appeared in respective Ag-composites, i.e., vibrations in CE, CH, and NA are remained in Ag-CE, Ag-CH, and in Ag-NA along with the presence of CH_2 vibration from CTAC capped Ag NCs. All the support materials contain an OH band in FT-IR, as shown in Fig. S4. The shape and position of these OH bands slightly varied after the incorporation of Ag NCs to support materials (Ag-composites). This change can be clearly seen in FT-IR and confirms the interaction of the OH group of support material with Ag NCs. Hence, FT-IR analysis confirms the adsorption of Ag NCs over CE, CH, and NA.

BET analysis was performed to know the surface area, pore diameter, and pore volume of support materials along with Ag-composites. Table S1 shows the materials (support materials and Ag-composites) and their respective surface area, pore diameter, and pore volume. CE shows a surface area of 0.968 m^2g^{-1} and Ag-CE shows a decrease in surface area (compare to CE) of 0.539 m^2g^{-1}. The decrease in the surface area of Ag-CE compared to CE is due to the adsorption of Ag NCs over bare CE. CH and Ag-CH exhibited surface areas of 20.672 and 0.763 m^2g^{-1}, respectively. The decrease in the surface area of Ag-CH compare to CH shows the good adsorption of Ag NCs. NA and Ag-NA provided with the surface area of 98.437 and 86.695 m^2g^{-1}, respectively. It is found that surface area is decreased in Ag-composites compared to their support materials. The decrease in pore size and volume of Ag-composites clearly suggests the adsorption of Ag NCs on support materials. CE, CH, and NA showed pore size of 10.4 nm,[38] 2.26 nm,[39] 10.9 nm,[40] respectively as mentioned in the literature. Hence, the pore size of CE, CH, and NA obtained in the present work is in well agreement with the reported value. The pore size was observed to decrease after the incorporation of Ag NCs (Table S1).This shows that Ag NCs were adsorbed on support materials. Ag-CE and Ag-CH samples are not porous, only Ag-NA composite showed good porous nature. As neutral alumina is a porous material, well porous nature is observed only for the Ag-NA. Zeta potential analysis was performed to understand the surface charge of the support materials and Ag-composites. Fig. S5A shows the zeta potential value of Ag NCs, support materials, and Ag-composites. Ag NCs exhibited a positive zeta potential of 19.2 mV as they are capped by CTAC (cationic surfactant). CE provided with -13.4 mV but when Ag NCs were added to CE it showed 9 mV. This change in the zeta potential value is because of the adsorption of Ag NCs over CE. CH and Ag-CH provided with zeta potential of -5.8 and -11.0 mV, respectively. NA and Ag-NA showed zeta potential of 22.3 and 29.5 mV, respectively. The change in the zeta potential value confirms the adsorption of Ag NCs over support materials in the Ag-composites. ICP-MS analysis was carried out to know the amount of Ag present in the Ag-composites. Fig. S5B, C, and D shows the ICP-MS values of Ag-CE, Ag-CH, and Ag-NA, respectively. ICP-MS values of 0.192, 0.190, and 0.171wt % correspond to Ag-CE, Ag-CH, and Ag-NA, respectively, confirms the very less loading of Ag NCs over support materials.

Raman and SERS analysis

The performance of the synthesized Ag-composites were tested for the detection of 4-MBA, R6G, and MB. For the detection of 4-MBA and R6G, 1mM analyte solution was added to three Ag-composites individually and analyzed for Raman analysis using 532 nm laser with 3 mW laser power, accumulation of 2 cycles, and acquisition time of 30 s employing 50X long working distance objective. Raman spectrum of bare 4-MBA (Fig. S6A) shows three major peaks at 1070, 1179, and 1583 cm^{-1} corresponding to the ring-breathing mode of C-C stretching (υ), deformation (δ) of C-H, and C-C ring stretching, respectively.[41] Bare 4-MBA and 4-MBA adsorbed Ag-composites (Ag-composites-4-MBA) exhibit same spectral positions with slight shifting after interaction with Ag-composites. The peaks at 1080 and 1583 cm^{-1} represent ring-breathing modes of C-C. COO- stretching observed at 1375 cm^{-1} and peak at 1470 cm^{-1} is attributed to combination modes of υ (CC) + δ (CH).[41,42] The peak position explained above is observed for 4-MBA adsorbed Ag-CE (Ag-CE-4-MBA). 4-MBA adsorbed Ag-CH (Ag-CH-4-MBA) and 4-MBA adsorbed Ag-NA (Ag-NA-4-MBA) also provided with the same Raman shift with slight variation in position. The intense peak observed at 1375 cm^{-1} in Ag-CE-4-MBA compared to Ag-CH-4-MBA and Ag-NA-4-MBA is due to the strong adsorption of 4-MBA in Ag-CE composite. Raman analysis of Ag-CE-4-MBA, Ag-CH-4-MBA, and Ag-NA-4-MBA are shown in Fig. S6B, C, and D, respectively. Table S2 shows the Raman peak assignments of 4-MBA with and without Ag-composites.[41,42] R6G was added to three Ag-composites individually and analyzed for Raman detection. The R6G adsorbed on Ag-composites (Ag-composites-R6G) showed peak at 608 cm^{-1} corresponds to C-C-C ring in-plane bending.[43] Peaks at 770 and 1122 cm^{-1} are assigned to C-H out-of-plane and C-H in-plane bending, respectively. C-O-C stretching peak was observed at 1293 cm^{-1}. The peak at 1365, 1505, 1568, and 1649 cm^{-1} are attributed to aromatic C-C stretching.[43] Raman spectra of R6G (1mM) with Ag-CE, Ag-CH, and Ag-NA are shown in Fig. S7. Table S3 depicts the peak assignments of R6G in Raman analysis.

Raman spectrum of bare MB (1 mM) is shown in Fig. 4A. All the peak assignment for Raman spectra of MB is tabulated in Table S4.[44] A strong peak that appeared at 448 cm^{-1} corresponds to skeletal deformation of C-N-C, 599 cm^{-1} peak represents skeletal deformation of C-S-C. 674 cm^{-1} peak in Raman spectra is assigned for out-of-plane bending of C-H (Fig. 4A).[44] In-plane ring deformation of C-H is observed at 1301 cm^{-1}. 1627 cm^{-1} is the ring stretching of C-C in MB

molecule (Fig. 4A).[44] Raman analysis of bare MB was measured by irradiation of 638 nm laser with 3 mW laser power, accumulation of 2 cycles, and acquisition time of 30 s.

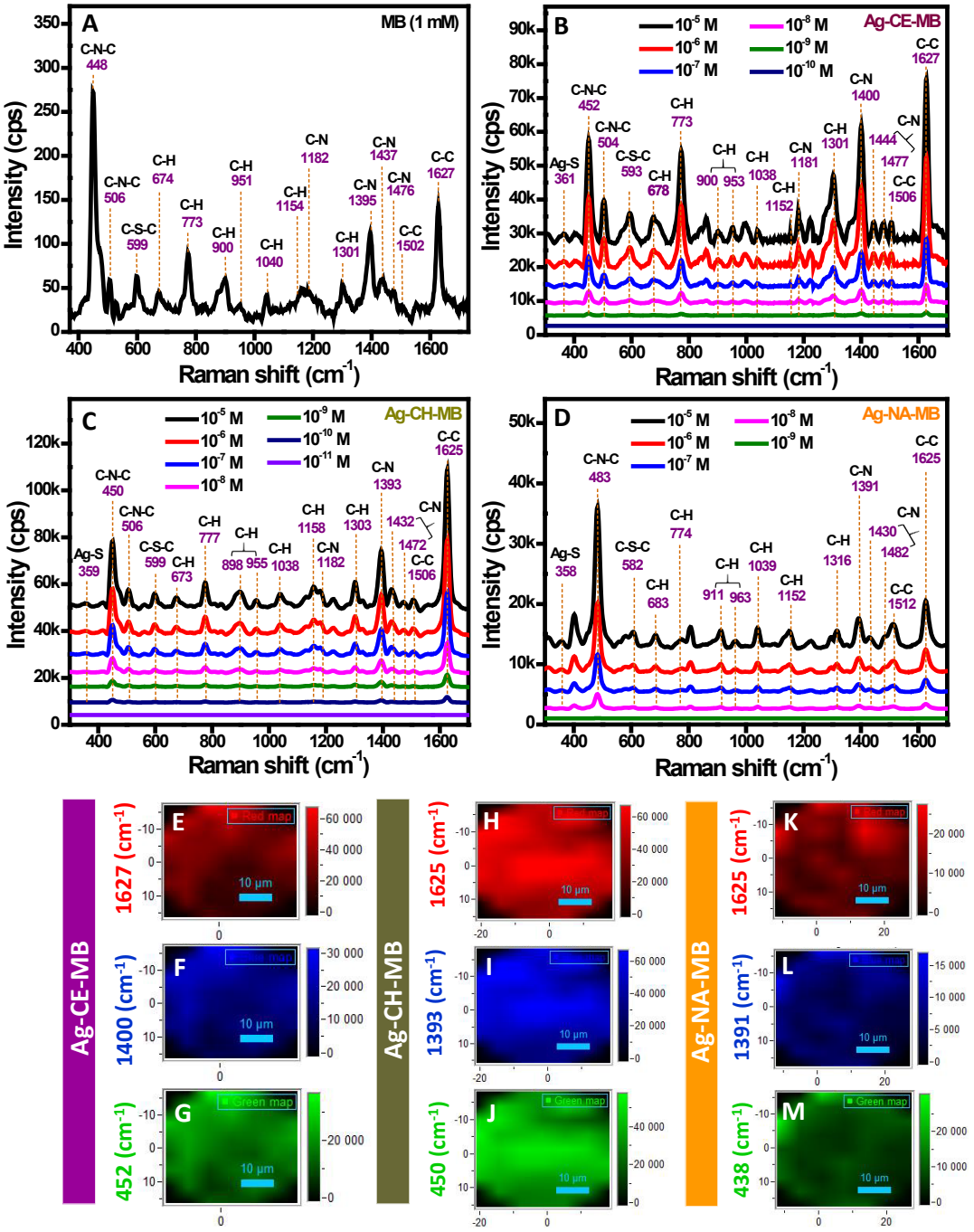

Figure 4. (A) Raman spectrum of bare MB (1 mM), SERS spectra of (B) Ag-CE-MB, (C)Ag-CH-MB, and (D) Ag-NA-MB. Raman mapping of MB (10 µM) with three Ag-composites (E-G) Ag-CE, (H-J) Ag-CH, and (K-M) Ag-NA for three different spectral positions.

SERS analysis has been performed only for MB as it provided more intensity spectra compared to other analytes. Bare MB and MB adsorbed Ag-composites (Ag-composites-MB) samples were normalized using 532 and 638 nm lasers. Normalization of laser with 532 and 638 nm laser wavelength for bare MB is shown in Fig. S8A and for the three Ag-composites as shown in Fig. S8B. From the laser normalization, it is seen that 638 nm laser provided with better enhancement compare to 532 nm laser. This is because the maximum absorption peak of MB lies at 664 nm which matches with the irradiated laser wavelength. Hence, 638 nm laser is kept constant to measure all SERS samples with 0.3 mW laser power, accumulation of 2 cycles, and acquisition time of 30 s. SERS spectra of MB adsorbed Ag-CE (Ag-CE-MB), MB adsorbed Ag-CH (Ag-CH-MB), and MB adsorbed Ag-NA (Ag-NA-MB) were shown in Fig. 4B, C, and D, respectively. Ag-CE, Ag-CH, and Ag-NA composites were able to detect MB at the concentration of 1 nM, 100 pM, and 100 µM, respectively. Beyond these concentrations, it was unable to obtain characteristic spectra of MB. Hence, the LOD for the MB in case of Ag-CE, Ag-CH, and Ag-NA is found to be 1 nM, 100 pM, and 100 µM, respectively. Ag-CH provided more intensity spectra followed by Ag-CE and Ag-NA for MB detection. So, Ag-CH showed better performance and sensitivity in the detection of MB. All the peak assignments for MB-adsorbed Ag-composites are tabulated in Table S4.[44]

Table 1 is tabulated for varieties of composites synthesized with different concentrations of Ag and LOD obtained for MB detection in earlier reports are compared with the present work. This comparison highlights that the present work incorporates very less concentration of Ag to the support material and successfully detected MB as low as 100 pM in the case of Ag-CH. It is observed that most of the spectral positions remain almost the same (in some spectra, slight shifting of 3-5 cm^{-1} is observed) in SERS analysis compared to bare Raman of MB. In case of Ag-CE-MB and Ag-CH-MB, the intensity of the peak at 448 cm^{-1} is decreased in SERS and it was the strongest peak in bare Raman along with the increase in intensity of peak at 1627 cm^{-1} is observed in SERS. But in the case of Ag-NA-MB, peaks at 506 and 1182 cm^{-1} assigned for skeletal deformation of C-N-C and stretching of C-N were disappeared in SERS and no futher significant changes were observed compared to Raman spectra of bare MB. In case of Ag-CE and Ag-CH, N-atom in the skeletal ring may have weak interaction with CE and CH of Ag-CE and Ag-CH and thus the decrease in the peak intensity was observed at 448 cm^{-1} (C-N-C). The important aspect is the

appearance of new peak at 361, 359, and 358 cm^{-1} are assigned for Ag-S vibration in Ag-CE-MB, Ag-CH-MB, and Ag-NA-MB, respectively. This shows that MB molecule is adsorbed on Ag-composites by the formation of Ag-S bond. In general, Ag-S bond vibration appears in the range of 330-340 cm^{-1},[6] however, the presence of support material in the Ag-composites, the Ag-S bond position slightly varied. The Ag-S bond formation is further confirmed by DFT analysis as explained in the computational section.As both support material and Ag NCs are present in composite, it is very important to know the main component which is responsible for the sensing of MB via SERS. For this reason, 1 µM MB (1 mL) was added individually to Ag NCs (20 µL) and bare support materials: CE, CH, and NA, and Raman analysis was performed by following the earlier sample preparation metioned above. Ag NCs-MB provided with nearly 18,850 counts, shown in Fig. S9A. Even though MB concentration was high, the bare support materials were unable to produce any characteristic spectra of MB. Fig. S9B is displayed with Raman spectra of 1 µM MB with three support materials and represented as CE-MB, CH-MB, and NA-MB. Hence, this study confirms that bare support materials were unable to detect MB via SERS. Even though Ag NCs-MB provided with good intensity spectra, but not better than Ag-composite substrates (Fig. 4B, C, and D). Hence, it is believed that due to the strong supportive nature of support materials for adsorption of Ag NCs, MB was detected at low concentration with very low loading of Ag NCs. Use of composites is the better option in view of environmental safety, cost-effectiveness, recyclability, and large-scale industrial use.

Enhancement factor calculation (EF)

$$EF = \frac{I_{SERS}/C_{SERS}}{I_{Raman}/C_{Raman}} \ldots\ldots\ldots (1)$$

Where,

I_{SERS} = Raman intensities of MB molecules in the SERS sample (Ag composite-MB)

I_{Raman} = Raman intensities of bare MB (1 mM),

C_{SERS} = Concentration of MB solution contributing to I_{SERS}

C_{Raman} = Concentration of MB solution contributing to I_{Raman}

Enhancement factor (EF) is calculated using equation (1).[4] The detailed EF calculation for Ag-CE-MB, Ag-CH-MB, and Ag-NA-MB shown in SI (enhancement factor calculation section). For the EF calculation, Raman spectral intensity of 1 mM bare MB is considered with Ag-composites containing 1 μM MB. EF for Ag-CE-MB, Ag-CH-MB, and Ag-NA-MB were found to be 1.2 x 10^6, 1.4 x $10^{6,}$ and 3.7 x 10^5, respectively. Raman mapping analysis has been performed to know the way of distribution of MB over Ag-composites. For the Raman mapping, MB of 10 μM with three Ag-composites was selected. Fig. 4E-G are the Raman mapping of Ag-CE-MB, where three spectral positions: 1627(Fig. 4E), 1400 (Fig. 4F), and 452 cm^{-1} (Fig. 4G) were selected. Fig. 4H, I, and J represent 1625, 1393, and 450 cm^{-1} peaks of Ag-CH-MB, respectively, in Raman mapping. The three peaks of Fig. 4K, L, and M represent Raman mapping for 1625, 1391, and 438 cm^{-1} peaks of Ag-NA-MB, respectively. There is a scale bar provided with each Raman mapping image with an increase in intensity. The bottom of the scale bar represents lower intensity with dark color (almost black) representation and the upper portion of the scale bar represents higher intensity with lighter color depiction. From the Raman mapping of Ag-composites-MB, it is clearly seen that the color distribution is nearly uniform in all three selected spectral positions. In Ag-CH-MB, the light color distribution is more followed by Ag-CE-MB and Ag-NA-MB. This shows that MB is more adsorbed over Ag-CH compared to the other two Ag-composites. Hence, Ag-CH provided with more enhancement for the detection of MB compared to other Ag-composites. These results matched with the intensity count and LOD obtained from SERS in proving Ag-CH is the better substrate for MB adsorbtion compared to the other two Ag-composites.

A uniformity study was done by selecting 15 random spots on the Ag-composites-MB to know the uniform adsorbtion of MB. Here, MB of 1 μM concentration is considered with all Ag-composites. Fig. S10A, B, and C represent the uniformity study on Ag-CE-MB, Ag-CH-MB, and Ag-NA-MB, respectively. Uniformity study reveals that the spectral intensities obtained from different random spots are nearly comparable in all three Ag-composites. Hence, the MB is uniformly adsorbed on Ag-composites, and Ag-composites behave as good SERS substrates. Relative standard deviation (RSD) calculation was measured from uniformity study and shown in Fig. S11. Ag-CE-MB (Fig. S11A), Ag-CH-MB (Fig. S11B), and Ag-NA-MB (Fig. S11C) provided with RSD values of 9.7, 8.6 and 12.9%, respectively. These RSD values show that the obtained intensity values are not much deviated from the mean value. Fig. S12A represents error bar calculation for 10^{-5} to 10^{-9} M

concentrations of MB with Ag-CE. The error bar for Ag-CH with MB of 10^{-5} to 10^{-10} M concentrations is shown in Fig. S12B. Fig. S12C shows the error bar for Ag-NA with MB of 10^{-5} to 10^{-8} M concentrations. Error bars were calculated from the values obtained by repeating SERS analysis five times. From this, we can see that the values in all five times are comparable for three Ag-composites.

Table 1. Different composites synthesized with different concentrations of Ag and LOD obtained for MB detection in earlier reports are compared with the present work.

Sl. No.	**Composites**	**Concentration of Ag (M)**	**LOD (M)**	**References**
1	Ag NPs-RGO	10	10^{-8}	19
2	MWCNTs-Ag	10×10^{-3}	10^{-7}	20
3	Fe_3O_4/GO/Ag	14.7×10^{-3}	10^{-9}	21
4	Ag NCs@PDMS	1.3×10^{-3}	10^{-9}	22
5	Ag coated magnetic polymethacrylate core-shell NPs	70.6×10^{-6}	10^{-7}	23
6	AgNPs/GO/g-CN	1×10^{-3}	10^{-12}	45
7	ZnO/Ag	0.2	10^{-9}	46
8	Paper/Ag NPs	1.05×10^{-3}	2×10^{-8}	47
9	**Ag-CE**	$\mathbf{0.18 \times 10^{-9}}$	$\mathbf{10^{-9}}$	**Present work**
10	**Ag-CH**	$\mathbf{0.18 \times 10^{-9}}$	$\mathbf{10^{-10}}$	**Present work**
11	**Ag-NA**	$\mathbf{0.18 \times 10^{-9}}$	$\mathbf{10^{-8}}$	**Present work**

X-ray photoelectron spectroscopy (XPS) analysis reveals the elemental composition and valence states of the samples. Ag NCs and all Ag-composites were subjected to XPS analysis, shown in Fig. 5. XPS survey spectra of Ag NCs, Ag-CE, Ag-CH, and Ag-NA are shown in Fig. 5A. Survey spectra of Ag NCs show peaks at 402.07 and 286.08 eV corresponding to N 1s and C 1s, respectively. Peaks observed at 374.10 and 368.10 eV are corresponding to Ag $3d_{3/2}$ and Ag $3d_{5/2}$, respectively.[48] The presence of C 1s and N 1s in the survey spectra of Ag NCs is because of the CTAC (CTAC stabilized Ag NCs), and it contains C and N. All the Ag-composites exhibit peaks at 533.08 and 286.08 eV attributed to O 1s and C 1s, respectively.[49] As CH contains N, the peak

that appeared at 402.07 eV corresponds to N 1s in Ag-CH. N 1s peak is also observed in case of Ag-NA, this is because of the presence of CTAC stabilized Ag NCs. All the spectral details are matched with the literature.[48,49] The marked position in survey spectra is for Ag 3d and shown as high-resolution spectra for Ag NCs, Ag-CE, Ag-CH, and Ag-NA in Fig. 5B, C, D, and E, respectively. For high-resolution spectra of Ag NCs, peaks observed at 374.10 and 368.10 eV corresponds to a doublet of Ag $3d_{3/2}$ and $3d_{5/2}$, respectively with spin-orbit coupling, $\Delta = 6.0$ eV (Fig. 5B). All the Ag-composites contain Ag NCs and only the peak position for Ag is shown in high-resolution spectra. Ag $3d_{3/2}$ and $3d_{5/2}$ peaks were observed at 374.10 and 368.10 eV for all Ag-composites, confirming the adsorption of Ag NCs over support material in Ag-composites (Fig. 5C, D, and E). Fig. 5F shows the table of all mentioned elements with respective binding energy.

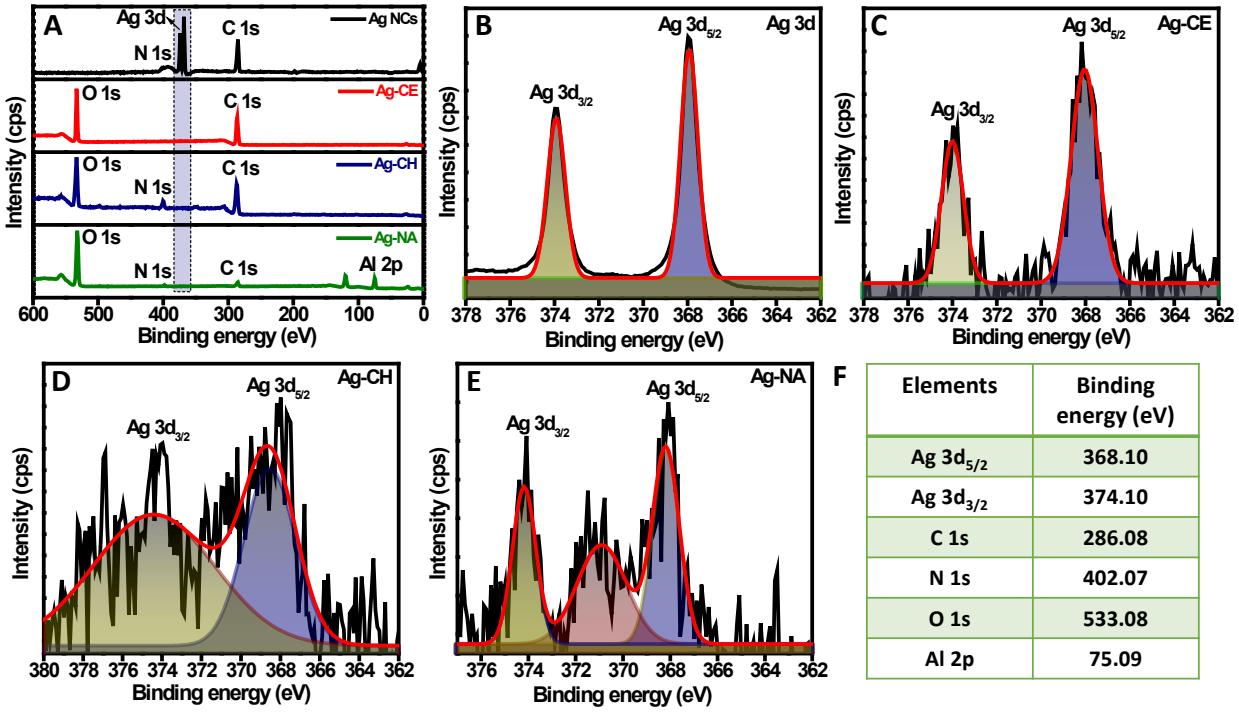

Elements	Binding energy (eV)
Ag $3d_{5/2}$	368.10
Ag $3d_{3/2}$	374.10
C 1s	286.08
N 1s	402.07
O 1s	533.08
Al 2p	75.09

Figure 5. (A) XPS survey spectra Ag NCs, Ag-CE, Ag-CH, and Ag-NA. High-resolution spectra of (B) Ag NCs, (C) Ag-CE, (D) Ag-CH, and (E) Ag-NA, and (F) Table composed of elements with binding energy.

Computational details

DFT studies

All calculations were carried out using spin polarized density functional theory (DFT) as implemented in VASP (Vienna Ab Initio Simulation Package) code[50] with projector augmented wave (PAW)[51] potential and Perdew-Burke-Ernzerhof (PBE)[52] functional of generalized gradient approximation (GGA). The convergence criterion for the plane-wave kinetic energy cut-off was set to 450 eV for all calculations. The convergence criteria of energy and force are 10^{-5} eV and 0.05 eV/Å, respectively. The Ag (111) and Ag (100) facets were modelled by (5 x 5) supercell consisting of repeated three-layer slabs. The Brillouin zone was sampled by a Monkhorst-Pack scheme[53] with 1 x 1 x 1 k-points grid for geometry optimization and single-molecule adsorption calculations. The DFT-D2[54] method is applied to describe the van der Waals interactions. The initial arrangements for the adsorbed molecules (CE, CH, and NA) on Ag surfaces were chosen to mimic the considered experimental findings, in which the molecules were hinted as preferring the lying-down structure on Ag surfaces. The optimizations of initial structures were performed via locating the O atoms of the molecules (CE, CH, and NA) on different active sites of various Ag facets. During the total energy calculations, the adsorbed molecule and the top layer of Ag atoms were allowed to relax in their positions to reach the most stable configuration, whereas Ag atoms of bottom layers were frozen to reduce the computational cost.

Further, we computed the adsorption energies of molecules (CE, CH, and NA) on Ag surfaces with different facets ((100) and (111)). The adsorption energies (E_{ad}) of molecules was computed by using the following equation (2).[55]

$$\mathbf{E_{ad} = E_{adsorbed\ system} - E_{system} - E_{free\ molecule}} \ldots\ldots (2)$$

Where, $E_{adsorbed\ system}$ is the total energy of surface with molecule, E_{system} is the total energy of surface and $E_{free\ molecule}$ is the total energy of free molecule. Using this equation, the negative values of E_{ad} suggest that adsorption of free molecules on the Ag surfaces are energetically favorable.

The charge density difference can be defined using equation (3),

$$\Delta\rho = \rho_{MB+composite} - \rho_{composite} - \rho_{MB} \ldots\ldots\ldots\ldots (3)$$

Where, $\rho_{MB+composite}$ is the total charge density of the system, $\rho_{composite}$ is the charge density of composite and ρ_{MB} is the charge density of free molecule.

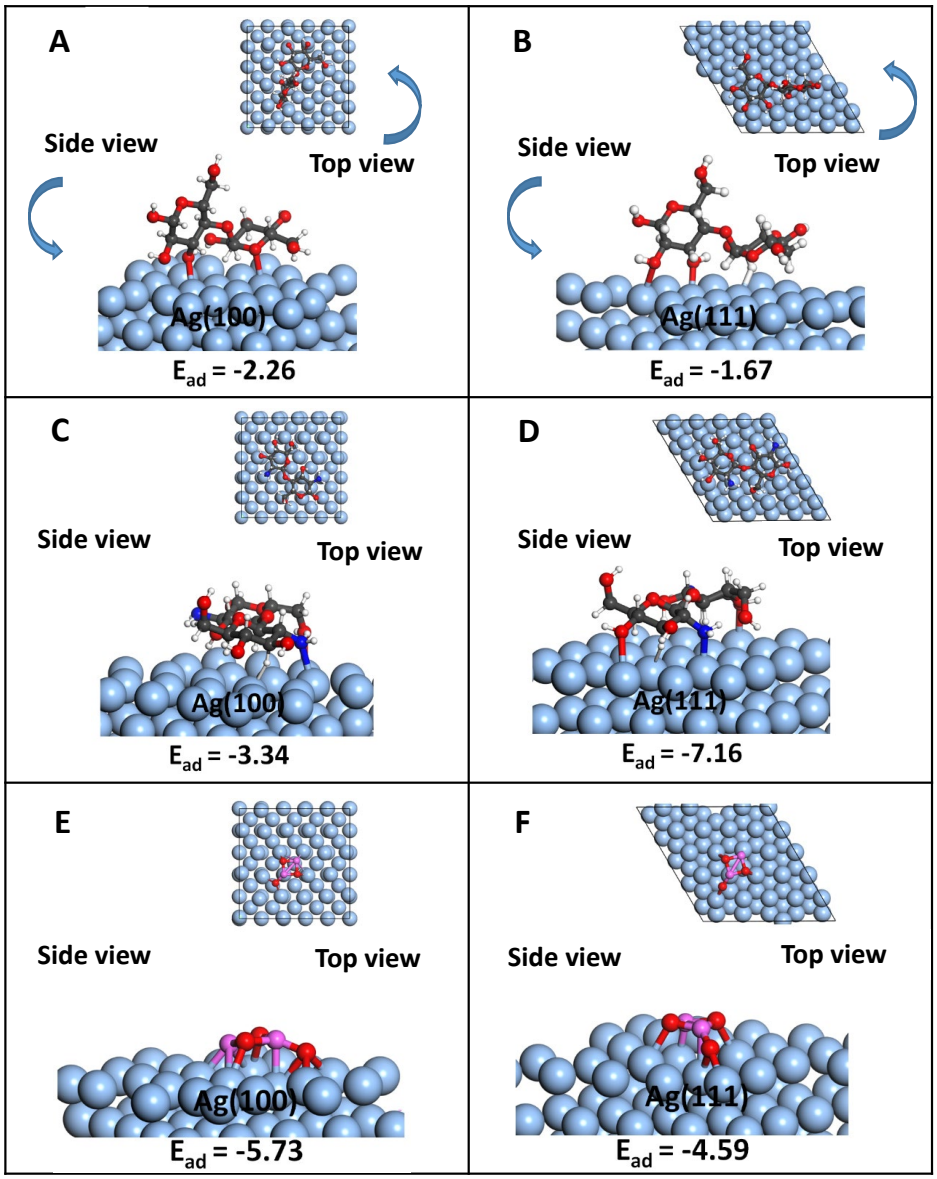

Figure 6. Optimized model structures of molecules adsorbed on different facets of Ag-NCs (A) Ag-CE (100), (B) Ag-CE (111), (C) Ag-CH (100), (D) Ag-CH (111), (E) Ag-NA (100), and (F) Ag-NA (111). Adsorption energies are given below for each model. All values are in eV.

The density functional theory (DFT) calculations were performed to first understand the configuration and facet selectivity for interaction between molecules (CE, CH, NA) and different Ag facets (As Ag NCs consist of (100) and (111) facets) (Fig. S13). G. Yao et al. attempted to figure out the conformations of simple rigid molecules on the surface of metal nanoparticles using Gaussian software to evaluate DFT-simulated Raman spectra.[56,57]

In the present work, the Vienna Ab initio Simulation Package (VASP) is used for simulation, where the Molecular Dynamics (MD) method is computationally costly. Thus, to achieve the research objective and to reduce the cost of calculations, we consider the most favorable geometrical conformation in this study, as reported in previous works.[58-60] Results reveal that the most probable configurations for the molecules (CE, CH, and NA) adsorbed on Ag surfaces are the lying-down geometry with O atoms of molecules occupying mostly the atop site and hollow site on different Ag facets (Fig. 6A-F). The distance between Ag atoms bonded to the adsorbed O atoms, N atom, H atom and Al atom are less (2.0-2.7 Å) (Table 2), implying the strong chemisorption between molecules and the Ag surfaces. Remarkably, the adsorption energy of CE, CH, and NA molecules on Ag (111), Ag (100), and Ag (111) facets is much lower than that for the Ag (100), Ag (111), and Ag (100) facets, respectively. Table 2 gives more details on bond length and adsorption energy of molecules and MB. This indicates that CE, CH and NA molecules possess unique facet selectivity for Ag (100) and Ag (111), hindering the deposition of Ag atoms and eventually leading to the formation of (100), (111), and (100) facet-terminated NCs on CE, CH, and NA, respectively.

Table 2. Bond length between different Ag atoms and oxygen atoms (Ag-O), nitrogen atom (Ag-N), hydrogen atom (Ag-H), and aluminium atom (Ag-Al). Adsorption energy values of molecules adsorbed on different facets of Ag and adsorption energy values of MB adsorbed on most stable composite is given. All values are in eV.

Surface	Bond Length (Å)	Adsorption Energy Molecules (E_{ad}) (eV)	Adsorption Energy of MB (E_{ad}) (eV)
Ag-CE (100)	2.62 (Ag-O),	-2.26	-5.57
Ag-CE (111)	2.67 (Ag-O),	-1.67	--
Ag-CH (100)	2.50 (Ag-O), 2.54 (Ag-N), 2.15 (Ag-H)	-3.34	--
Ag-CH (111)	2.65 (Ag-O), 2.34 (Ag-N), 2.00 (Ag-H)	-7.16	-5.98

Ag-NA (100)	2.42 (Ag-O), 2.47 (Ag-Al)	-5.73	-5.30
Ag-NA (111)	2.50 (O-Ag), 2.64 (Ag-Al)	-4.59	--

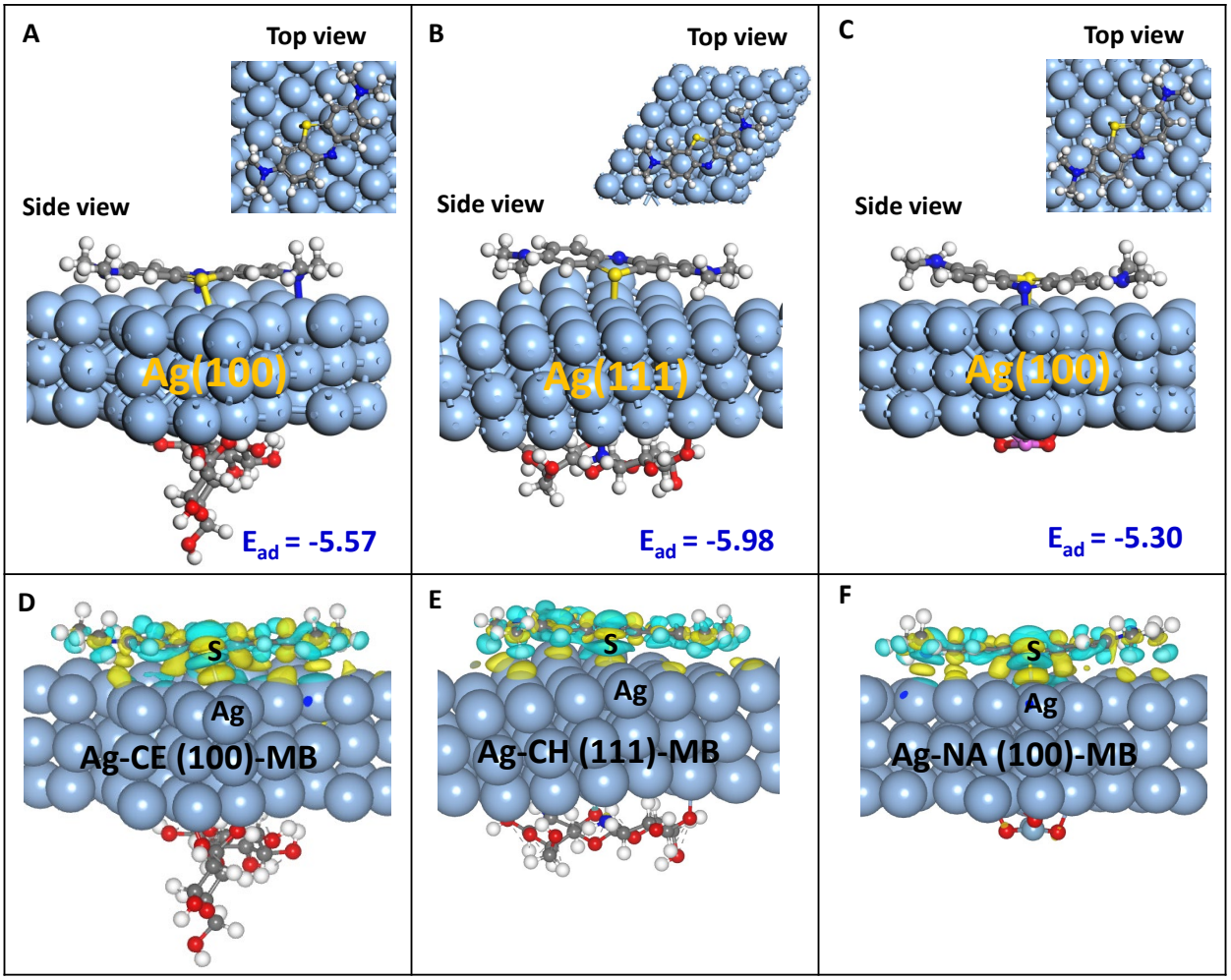

Figure 7.Optimized model structures of different composite adsorbed with MB (A) Ag-CE (100)-MB, (B) Ag-CH (111)-MB, and (C) Ag-NA (100)-MB. Top view of the structures are given in inset. (D-F).Charge density difference of the MB molecule adsorbed on Ag facets. Blue and yellow color represent charge loss and charge accumulation, respectively. For clarity, the S and Ag atoms are marked.

Further, to check the detection of hazardous analyte such as MB, we only considered (100), (111), and (100) facet-terminated Ag NCs on CE, CH, and NA, respectively. The calculated adsorption energies for MB with Ag NCs on CE, CH, and NA molecules are -5.57 eV, -5.98 eV, and -5.30 eV, respectively (Table 2). Optimized structures are shown in Fig. 7A-C, where the sulfur atom of MB

is strongly interacting with the composite and adsorbed in atop configuration on Ag atom. The charge density difference of MB adsorbed on the Ag facets with most stable structure is shown in Fig. 7D-F. As a result of the MB molecule's chemical adsorption and the resulting redistribution of charge density in the MB molecule, the electronic structures of the Ag facets are altered. Electrons tend to accumulate around S atoms, C atoms of the C=S functional group of MB molecules and the Ag surface nearby, as shown in Fig. 7D-F. Results indicate that when a MB molecule is adsorbed on electron rich Ag facets, electrons may transfer from surface of Ag atoms to MB molecule. This electron transfer is majorly dependent on the Ag surface structure. Hence, all adsorption configuration is energetically favorable but MB can be highly detected by (111) terminated Ag-CH composite than Ag-CE and Ag-NA. Order of detection efficiency of MB can be given according to the binding energy which is, Ag-CH > Ag-CE > Ag-NA. Results indicate that the theoretical study is matching well with the experimental outcome. From theoretical analysis, it can be concluded that Ag-CH composite is more sensitive towards MB with better adsorption energy, therefore, this type of composite materials are highly suitable for detection of environmentally hazardous contaminants.

Finite-Difference Time-Domain Simulation

3D finite-difference time-domain (FDTD) calculation was performed using Lumerical FDTD simulation software. Ag NC of side length 45nm and diagonal length 65nm on a glass substrate of 1mm thick were considered for simulation. Simulations are carried out on single, dimer, and trimer Ag NC configurations keeping a gap of 4 nm as shown in Fig. 8. A plane wave was used for excitation, propagating along the negative z-axis direction with 0° polarization. The excitation wavelength and size of the nanostructure greatly impacts on the electric field distribution in FDTD.[61,62] The laser wavelength used was centered at 632nm. All output images were optimized and normalized to the intensity of the excitation source. Periodic boundary conditions were applied in the plane of the simulated structure. The frequency-dependent dielectric function of Ag was taken from literature[63] and the effective refractive index of the surrounding dielectric was set to 1.33.

The field enhancement observed in the SERS experiments with the Ag NCs are compared with the results from FDTD simulations with three different configurations. Fig. 8A-C display the electric

field intensity distributions for the selected geometries. Three different geometrical configurations of the NCs corresponding to experimentally observed structures (Ag NCs with rounded corners, radius of curvature: 3 nm) were considered for modeling.

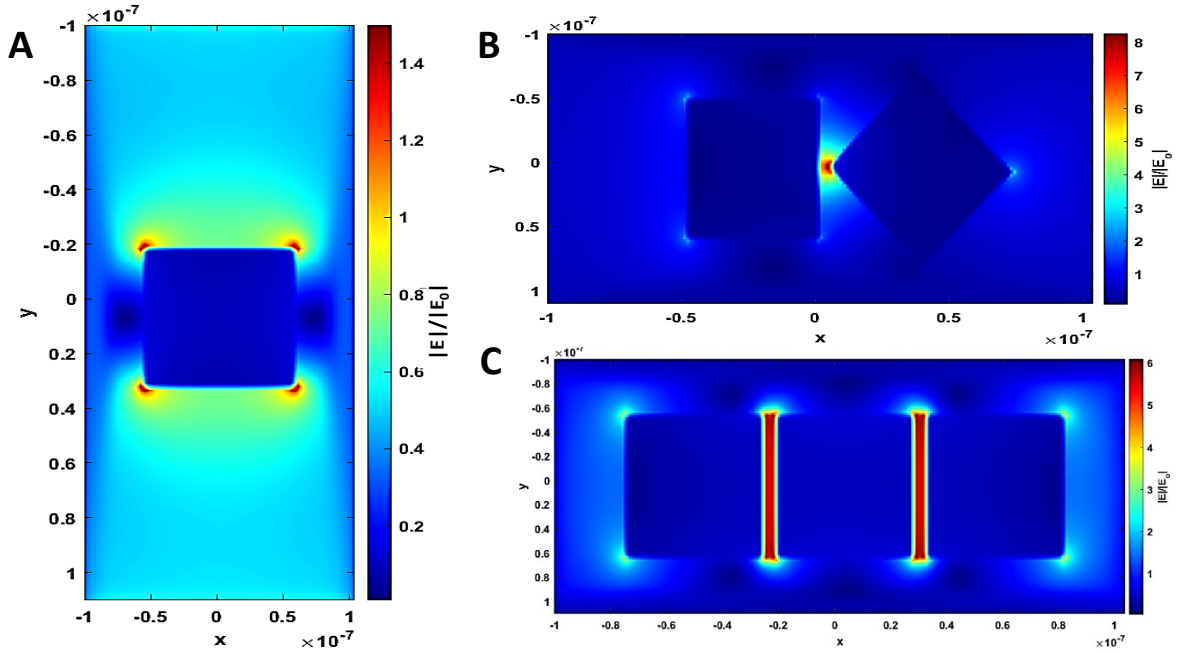

Figure 8. Simulated (3D-FDTD) electric field intensity distribution in the xy-plane for three geometrical configurations of the NCs corresponding to experimentally observed structures (Ag NCs with rounded corners, radius of curvature: 3 nm). (A) Single Ag NC, (B) face-to-edge Ag NCs dimers (one nanocube rotated by 90^0), and (C) face-to-face Ag NCs trimers.

Fig. 8A, B, and C display three different geometries namely, single Ag NC, face-to-edge Ag NCs dimers (one nanocube rotated by 90^0),and face-to-face Ag NCs trimers, respectively. The distribution of electric field intensity is provided for each configuration. For a single Ag NC, the highest electric field is observed at the corners (red color) (Fig. 8A), as reported in literature.[64] Considering equal conditions for the excitation and the scattering field, it would lead to an electromagnetic SERS enhancement of ~1.4×10^2.Fig. 8B and C indicate that, when aggregates are formed on the glass, the electric field enhancement increases significantly, and the highest field enhancement is localized at the corners and in the nanogaps between the NCs in both the configurations. For face-to-edge Ag NCs dimers, electric field intensity distribution is more at the contact of two Ag NCs (face of one Ag NC to the edge of another Ag NC) and for face-to-face Ag NCs trimers the electric field intensity distribution is more at the nanogaps between the adjacent

Ag NCs. Face-to-edge Ag NCs dimers and face-to-face Ag NCs trimers exhibited EF of 8×10^6 and 6×10^6, respectively. EF for Ag-CE-MB, Ag-CH-MB, and Ag-NA-MB was found to be 1.2×10^6, 1.4×10^6, and 3.7×10^5, respectively via experimental method. As EF of Ag-CE-MB and Ag-CH-MB is in the order of 10^6, Ag NCs are expected to present mostly in dimer or trimer configurations. But in case of Ag-NA-MB, EF is in the order of 10^5, this may be due to the mixed Ag NC configurations of single, dimer and trimer. Upon the addition of Ag NCs to support materials, Ag NCs are arranged mostly in dimer and trimer form along with single NCs throughout the sample. FESEM and TEM analyses confirm the different arrangement configurations of Ag NCs in the composites, as shown in Fig. S1. In Fig. S1, blue, green, and orange markings represent the single, dimer, and trimer of Ag NCs, respectively, present in the different composites.

Plausible mechanism and real time filtration process

The plausible mechanism of MB adsorption on three Ag-composites shown in Fig. 9A and depicted based on the Raman, SERS, and DFT studies. From the SERS analysis, it is very clear that the MB molecules adsorbed on Ag-composites by direct bond formation with Ag NCs. Hence, new peak assigned to Ag-S was observed in SERS. Even though MB molecule is directly attached to Ag NCs, the role of support materials in the detection of MB cannot be neglected. Here, Sulfur atom of MB attached to Ag NCs, and the support materials can facilitate the adsorption of Ag NCs on them. This chain of adsorption property between support materials, Ag NCs, and MB can lead to the better detection of MB compared to bare Ag NCs (Fig. S9A). Hence, mechanism cannot be exactly synergistic effect between Ag NCs and support materials, because when MB molecule is measured on bare support materials, no significant spectra was obtained (Fig. S9B). But, the support materials may act as strong backbone for Ag NCs to adsorb MB. DFT studies depicts the interaction of support materials with Ag NCs and shows that the distance between Ag atoms bonded to the adsorbed O atoms, N atom, H atom and Al atom (from support materials) are less (2.0-2.7 Å) implying the strong chemisorption between support materials and the Ag surfaces. DFT studies also confirms the adsorption of MB on Ag-composites by Ag-S bond formation. Hence theoretical as well as experimental analyses were well matched and confirmed the formation of Ag-S bond between MB and Ag-composites. Charge density calculations specify that when a MB molecule is adsorbed on electron rich Ag facets, electrons transfer from surface of Ag atoms

to MB molecule. This electron transfer is strongly emphasizing the chemical enhancement along with electromagnetic enhancement in the system.

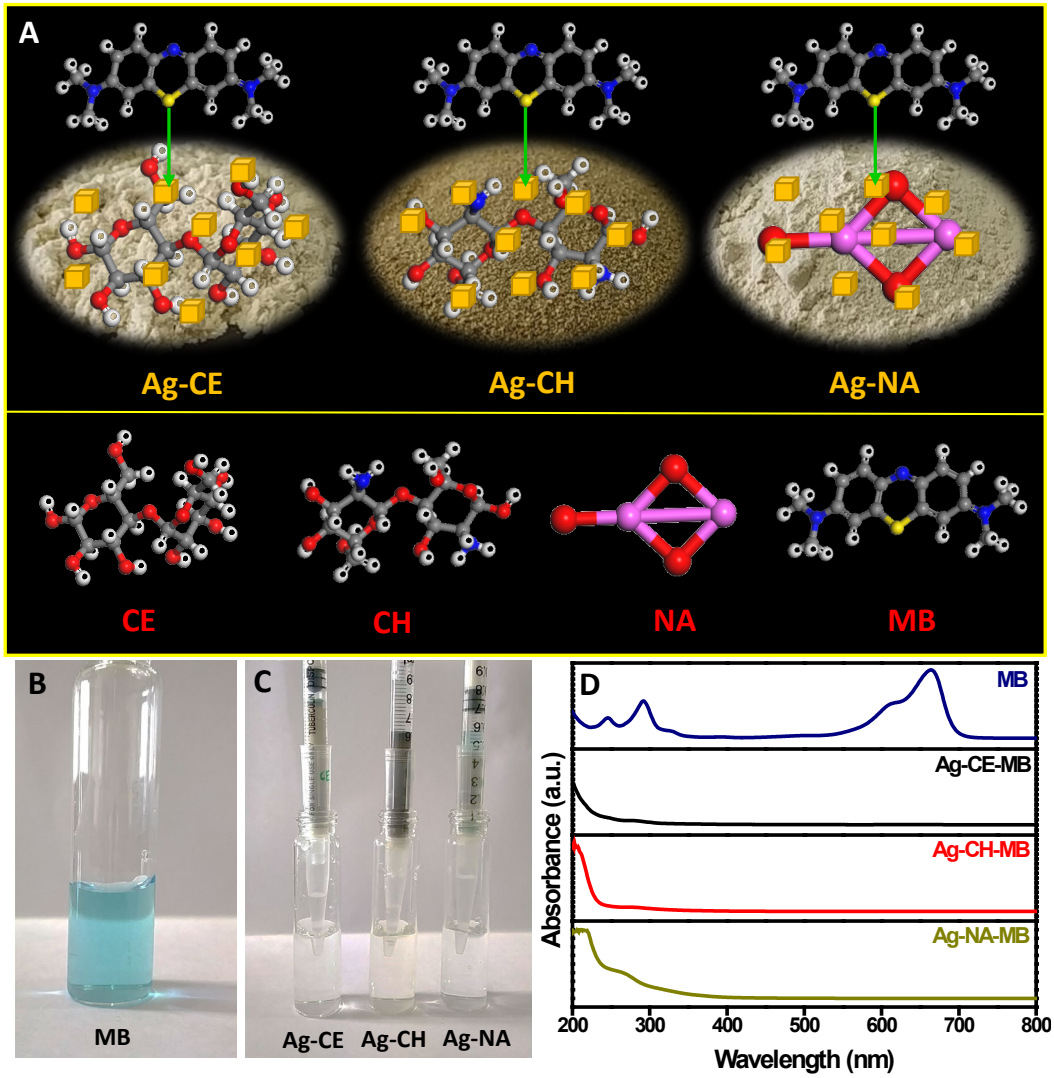

Figure 9. Plausible mechanism of adsorption of MB on (A) Ag-CE, Ag-CH, and Ag-NA.(B) MB (10 µM), (C) filtration unit for Ag-CE, Ag-CH, and Ag-NA, and (D) UV-vis absorption spectra of MB and the filtrate from Ag-CE, Ag-CH, and Ag-NA after passing MB from the filtration unit.

A real-time filtration unit was constructed by filling 1 g of the Ag-composites individually in the syringe tube. Initially, small cotton was placed in the syringe then 1 g of composite material was filled individually in three syringes. Further 3 mL of 10 µM MB solution was made to pass through the filtration unit. The filtrate that comes out of the filtration unit was collected and subjected to UV-vis analysis to confirm the MB adsorption. Real-time filtration unit is shown in Fig. 9. Fig.

9B shows the 10 μM MB, Fig. 9C shows the filtration unit for Ag-CE, Ag-CH, and Ag-NA after passing MB. Fig. 9D shows the UV-vis absorption spectra for 10 μM MB, filtrate collected from Ag-CE-MB, Ag-CH-MB, Ag-NA-MB. It is clearly seen in Fig. 9D that the filtrate from Ag-CE and Ag-CH does not contain MB but Ag-NA contains less concentration of MB. This shows Ag-CE and Ag-CH adsorbs MB completely, whereas Ag-NA was less better. Hence, Ag-CE and Ag-CH can be successfully employed for the real-time analysis for the filtration of MB to get pure water. This small scale can also be applied for large-scale filtration unitson an industrial scale.

Conclusion

Ag NCs were successfully synthesized and used for the preparation of three composites, Ag-CE, Ag-CH, and Ag-NA with 0.2 wt % of Ag NCs loading. All the Ag-composites were successfully characterized by XRD, FT-IR, FESEM, HRTEM, elemental mapping, EDS, line scan profile, zeta potential, ICP-MS, and XPS analysis.ICP-MS values well matched with the concentration of experimentally loaded Ag NCs with the support materials. MB was detected using all the Ag-composites through Raman analysis. EF for Ag-CE-MB, Ag-CH-MB, and Ag-NA-MB was found to be 1.2×10^6, 1.4×10^6, and 3.7×10^5, respectively. LOD of 1 nM, 100 pM, and 100 μM was achieved for Ag-CE, Ag-CH, and Ag-NA, respectively. All the samples exhibited good uniformity and RSD of 9.7, 8.6, and 12.9% for Ag-CE-MB, Ag-CH-MB, and Ag-NA-MB, respectively. MB was detected to ultra-low concentration due to the strong bonding of Ag NCs and support materials. DFT calculations reveal that configuration and facet selectivity for interaction between molecules CE, CH, and NA with different Ag facets. Order of detection efficiency of MB follows Ag-CH > Ag-CE > Ag-NA with respect to the binding energy. Hence, results from the theoretical study is well equivalent with the experimental outcome, where Ag-CH exhibited more sensitivity for MB detection. Charge density calculations confirm the strong adsorption of MB on Ag-composites. This shows the strong adsorption of MB on Ag-composites enables ultra-low detection via SERS. The EF values observed from FDTD simulation for single, dimer and trimer present in the Ag-composite are found to be 1.4×10^2, 8×10^6, and 6×10^6, respectively, and observed a maximum EF for face-to-edge configuration in dimer. A real-time filtration unit was made to filter MB with all three Ag-composites. Ag-CE and Ag-CH composites showed better adsorption of MB compared to Ag-NA. Hence, the filtration unit can be employed on an industrial scale for real-time analysis. Overall, the composite materials exhibit excellent performance for detection of

environmental hazardous contaminants and also meet the need of cost effectiveness, and environmental support materials.

Supporting information

Manuscript's supporting information (SI) is available online.

Materials and methods, Synthesis of Ag NCs, FESEM and TEM images of Ag-composites, Cumulative mapping and line scan profile of Ag-composites, TEM-EDS analysis of Ag-composites, FT-IR analysis of Ag NCs, support materials and Ag-composites, Table S1, Zeta potential and ICP-MS analysis of Ag-composites, Raman analysis of 4-MBA and Ag-composites-4-MBA, Table S2, Raman analysis of Ag-composites-R6G, Table S3, Table S4, Normalization of laser for MB and Ag-composites-MB, Raman analysis of MB with Ag NCs and support materials, Enhancement factor calculation, Uniformity study of Ag-composites-MB, RSD calculation for Ag-composites-MB, Error bar calculation for Ag-composites-MB, Optimized model structures of different facets in Ag-NCs

Acknowledgement

BMB acknowledges JAIN University for Junior Research Fellowship. AKS is grateful to the SERB, New Delhi, India for funding to conduct the research (CRG/2018/003533) and Karnataka Science and Technology Promotion Society (KSTePS/VGST-RGS-F/2018-19/GRD No.831/315). The authors thank Central Research Facility at CeNS for providing TEM and Confocal Raman microscope facility.

Conflicts of interest

The authors declare no competing financial interest.

References

(1) Ray, P. C.; Yu, H.; Fu, P. P. Toxicity and environmental risks of nanomaterials: challenges and future needs. *J. Environ. Sci. Health C* **2009**, *27* (1), 1-35.

(2) Bhavya, M. B.; Swain, S.; Bhol, P.; Yadav, S.; Altaee, A.; Saxena, M.; Misra, P. K.; Samal, A. K. Functionalized Nanomaterials (FNMs) for Environmental Applications. *Functionalized Nanomaterials for Catalytic Application.* Wiley Online Library **2021**, pp 109-134.

(3) Sanità, G.; Carrese, B.; Lamberti, A., Nanoparticle surface functionalization: how to improve biocompatibility and cellular internalization. *Front. Mol. Biosci.* **2020**, *7*, 587012.
(4) Khlebtsov, B. N.; Khanadeev, V. A.; Panfilova, E. V.; Bratashov, D. N.; Khlebtsov, N. G. Gold nanoisland films as reproducible SERS substrates for highly sensitive detection of fungicides. *ACS Appl. Mater. Interfaces* **2015**, *7* (12), 6518-6529.
(5) Bhavya M. B.; Manippady, S. R.; Saxena, M.; Ramya Prabhu B.; John, N. S.; Balakrishna, R. G.; Samal, A. K. Gold Nanorods as an efficient substrate for the detection and degradation of pesticides. *Langmuir* **2020**, *36* (26), 7332-7344.
(6) Bhavya, M. B.; Ramya Prabhu B.; M B. Shenoy, B. M.; Bhol, P.; Swain, S.; Saxena, M.; John, N. S.; Hegde, G.; Samal, A. K. Femtomolar detection of thiram via SERS using silver nanocubes as an efficient substrate. *Environ. Sci.: Nano* **2020**, *7* (12), 3999-4009.
(7) Bhavya, M. B.; Ramya Prabhu B.; Tripathi, A.; Yadav, S.; John, N. S.; Thapa, R.; Altaee, A.; Saxena, M.; Samal, A. K., A Unique Bridging Facet Assembly of Gold Nanorods for the Detection of Thiram through Surface-Enhanced Raman Scattering. *ACS Sustain. Chem. Eng.* **2022**, *10* (22), 7330–7340.
(8) Liu, Q.; Li, Y.; Chen, H.; Lu, J.; Yu, G.; Möslang, M.; Zhou, Y. Superior adsorption capacity of functionalised straw adsorbent for dyes and heavy-metal ions. *J. Hazard. Mater.* **2020**, *382*, 121040.
(9) Şen, S.; Demirer, G. Anaerobic treatment of real textile wastewater with a fluidized bed reactor. *Water Res.* **2003**, *37* (8), 1868-1878.
(10) Dos Santos, A. B.; Cervantes, F. J.; Van Lier, J. B. Review paper on current technologies for decolourisation of textile wastewaters: perspectives for anaerobic biotechnology. *Bioresour. Technol.* **2007**, *98* (12), 2369-2385.
(11) Liu, Q. Pollution and treatment of dye waste-water. In *IOP Conference Series: Earth Environ. Sci.* **2020**; IOP Publishing: Vol. 514, p 052001.
(12) Rashed, M. N. Adsorption technique for the removal of organic pollutants from water and wastewater. *Organic pollutants-monitoring, risk and treatment* **2013**, *7*, 167-194.
(13) Adusumalli, V. N. K. B.; Koppisetti, H. V. S. R. M.; Madhukar, N.; Mahalingam, V. 4-Mercaptobenzoic acid capped terbium (III)-doped CaF_2 nanocrystals: a fluorescent probe for nitroaromatic pollutants. *Microchim. Acta* **2019**, *186* (6), 1-9.

(14) Li, Y.; Xin, X.; Zhang, T.; Li, W.; Li, J.; Lu, R. Raspberry-like polyamide@Ag hybrid nanoarrays with flexible cores and SERS signal enhancement strategy for adenosine detection. *Chem. Eng. J.* **2021**, *422*, 129983.

(15) Shakoor, S.; Nasar, A. Adsorptive treatment of hazardous methylene blue dye from artificially contaminated water using cucumis sativus peel waste as a low-cost adsorbent. *Groundw. Sustain. Dev.* **2017**, *5*, 152-159.

(16) Kim, D.; Ko, Y.; Kwon, G.; Kim, U.-J.; Lee, J. H.; You, J. 2, 2, 6, 6-tetramethylpiperidine-1-oxy-oxidized cellulose nanofiber-based nanocomposite papers for facile in situ surface-enhanced Raman scattering detection. *ACS Sustain. Chem. Eng.* **2019**, *7* (18), 15640-15647.

(17) Li, J.; Tian, X.; Hua, T.; Fu, J.; Koo, M.; Chan, W.; Poon, T., Chitosan natural polymer material for improving antibacterial properties of textiles. *ACS Appl. Bio Mater.* **2021**, *4* (5), 4014-4038.

(18) Hulbert, S. The use of alumina and zirconia in surgical implants. *Advanced series in ceramics.*World Scientific **1993**, pp 25-40.

(19) Chettri, P.; Vendamani, V.; Tripathi, A.; Singh, M. K.; Pathak, A. P.; Tiwari, A. Green synthesis of silver nanoparticle-reduced graphene oxide using Psidium guajava and its application in SERS for the detection of methylene blue. *Appl. Surf. Sci.* **2017**, *406*, 312-318.

(20) Dinh, N. X.; Huy, T. Q.; Le, A.-T. Multiwalled carbon nanotubes/silver nanocomposite as effective SERS platform for detection of methylene blue dye in water. *J. Sci.: Adv. Mater. Devices* **2016**, *1* (1), 84-89.

(21) He, J.; Song, G.; Wang, X.; Zhou, L.; Li, J. Multifunctional magnetic Fe_3O_4/GO/Ag composite microspheres for SERS detection and catalytic degradation of methylene blue and ciprofloxacin. *J. Alloys Compd.* **2022**, *893*, 162226.

(22) Li, L.; Chin, W. S. Rapid fabrication of a flexible and transparent Ag nanocubes@PDMS film as a SERS substrate with high performance. *ACS Appl. Mater. Interfaces* **2020**, *12* (33), 37538-37548.

(23) Kibar, G.; Topal, A. E.; Dana, A.; Tuncel, A. Newly designed silver coated-magnetic, monodisperse polymeric microbeads as SERS substrate for low-level detection of amoxicillin. *J. Mol. Struct.* **2016**, *1119*, 133-138.

(24) Ding, G.; Xie, S.; Liu, Y.; Wang, L.; Xu, F., Graphene oxide-silver nanocomposite as SERS substrate for dye detection: Effects of silver loading amount and composite dosage. *Appl. Surf. Sci.* **2015**, *345*, 310-318.

(25) Samodelova, M. V.; Kapitanova, O. O.; Evdokimov, P. V.; Eremina, O. E.; Goodilin, E. A.; Veselova, I. A., Plasmonic features of free-standing chitosan nanocomposite film with silver and graphene oxide for SERS applications. *Nanotechnology* **2022**, *33* (33), 335501.

(26) Zhou, S.; Li, J.; Gilroy, K. D.; Tao, J.; Zhu, C.; Yang, X.; Sun, X.; Xia, Y. Facile synthesis of silver nanocubes with sharp corners and edges in an aqueous solution. *ACS Nano* **2016**, *10* (11), 9861-9870.

(27) Klinkova, A.; Thérien-Aubin, H.; Ahmed, A.; Nykypanchuk, D.; Choueiri, R. M.; Gagnon, B.; Muntyanu, A.; Gang, O.; Walker, G. C.; Kumacheva, E., Structural and optical properties of self-assembled chains of plasmonic nanocubes. *Nano lett.* **2014**, *14* (11), 6314-6321.

(28) Sun, Y.; Xia, Y. Shape-controlled synthesis of gold and silver nanoparticles. *science* **2002**, *298* (5601), 2176-2179.

(29) Keshk, S. M. A. S.; Hamdy, M. S. Preparation and physicochemical characterization of zinc oxide/sodium cellulose composite for food packaging. *Turk. J. Chem.* **2019**, *43* (1), 94-105.

(30) Dey, S. C.; Al-Amin, M.; Rashid, T. U.; Sultan, M. Z.; Ashaduzzaman, M.; Sarker, M.; Shamsuddin, S. M. Preparation, characterization and performance evaluation of chitosan as an adsorbent for remazol red. *Int. J. latest Res. Eng. Technol.* **2016**, *2* (2), 52-62.

(31) Farahmandjou, M.; Golabiyan, N. New pore structure of nano-alumina (Al_2O_3) prepared by sol gel method. *J. Ceram. Process. Res.* **2015**, *16* (2), 1-4.

(32) Liu, Y.; Zhong, Q.; Zhang, T. Preparation of cationic surfactant intercalated graphene oxide and quantitative determination of the interlamellar spacing. *Fuller. Nanotub. Carbon Nanostructures* **2015**, *23* (3), 196-202.

(33) Atykyan, N.; Revin, V.; Shutova, V. Raman and FT-IR Spectroscopy investigation the cellulose structural differences from bacteria Gluconacetobacter sucrofermentans during the different regimes of cultivation on a molasses media. *AMB Express* **2020**, *10* (1), 1-11.

(34) Drabczyk, A.; Kudłacik-Kramarczyk, S.; Głąb, M.; Kędzierska, M.; Jaromin, A.; Mierzwiński, D.; Tyliszczak, B. Physicochemical investigations of chitosan-based hydrogels containing Aloe Vera designed for biomedical use. *Materials* **2020**, *13* (14), 3073.

(35) Yasmeen, S.; Kabiraz, M. K.; Saha, B.; Qadir, M.; Gafur, M.; Masum, S. Chromium (VI) ions removal from tannery effluent using chitosan-microcrystalline cellulose composite as adsorbent. *Int. Res. J. Pure Appl. Chem.* **2016**, *10* (4), 1-14.

(36) Wang, L.; Cavaco-Paulo, A.; Xu, B.; Martins, M. Polymeric hydrogel coating for modulating the shape of keratin fiber. *Front. Chem.* **2019**, *7*, 749.

(37) Liu, C.; Shih, K.; Gao, Y.; Li, F.; Wei, L. Dechlorinating transformation of propachlor through nucleophilic substitution by dithionite on the surface of alumina. *J. Soils Sediments* **2012**, *12* (5), 724-733.

(38) Tade, R. S.; More, M. P.; Chatap, V. K.; Patil, P. O.; Deshmukh, P. K., Fabrication and in vitro drug release characteristics of magnetic nanocellulose fiber composites for efficient delivery of nystatin. *Mater. Res. Express* **2018**, *5* (11), 116102.

(39) de Freitas, F. P.; Carvalho, A. M. M. L.; Carneiro, A. d. C. O.; de Magalhaes, M. A.; Xisto, M. F.; Canal, W. D., Adsorption of neutral red dye by chitosan and activated carbon composite films. *Heliyon* **2021**, *7* (7), e07629.

(40) Fatimah, T. S.; Wahyudi, T.; Khaerunisa, H.; Saleh, N. In Characterization of the γ, α-alumina and its adsorption capability to adsorb nickel (ii) and magnesium (ii) from nickel sulfate as a result of solvent differences, *IOP Conf. Ser. Mater. Sci. Eng.* IOP Publishing: **2021**; p 012151.

(41) Jiang, L.; You, T.; Yin, P.; Shang, Y.; Zhang, D.; Guo, L.; Yang, S. Surface-enhanced Raman scattering spectra of adsorbates on Cu 2 O nanospheres: charge-transfer and electromagnetic enhancement. *Nanoscale* **2013**, *5* (7), 2784-2789.

(42) Wiriyakun, N.; Pankhlueab, K.; Boonrungsiman, S.; Laocharoensuk, R. Site-selective controlled dealloying process of gold-silver nanowire array: a simple approach towards long-term stability and sensitivity improvement of SERS substrate. *Sci. Rep.* **2016**, *6* (1), 1-11.

(43) He, X. N.; Gao, Y.; Mahjouri-Samani, M.; Black, P.; Allen, J.; Mitchell, M.; Xiong, W.; Zhou, Y.; Jiang, L.; Lu, Y. Surface-enhanced Raman spectroscopy using gold-coated horizontally aligned carbon nanotubes. *Nanotechnology* **2012**, *23* (20), 205702.

(44) Li, C.; Huang, Y.; Lai, K.; Rasco, B. A.; Fan, Y. Analysis of trace methylene blue in fish muscles using ultra-sensitive surface-enhanced Raman spectroscopy. *Food Control* **2016**, *65*, 99-105.

(45) Santhoshkumar, S.; Murugan, E., Rationally designed SERS AgNPs/GO/g-CN nanohybrids to detect methylene blue and Hg^{2+} ions in aqueous solution. *Appl. Surf. Sci.* **2021**, *553*, 149544.

(46) Pham, T. T. H.; Vu, X. H.; Dien, N. D.; Trang, T. T.; Chi, T. T. K.; Phuong, P. H.; Nghia, N. T., Ag nanoparticles on ZnO nanoplates as a hybrid SERS-active substrate for trace detection of methylene blue. *RSC adv.* **2022,** *12* (13), 7850-7863.
(47) Yang, G.; Fang, X.; Jia, Q.; Gu, H.; Li, Y.; Han, C.; Qu, L.-L., Fabrication of paper-based SERS substrates by spraying silver and gold nanoparticles for SERS determination of malachite green, methylene blue, and crystal violet in fish. *Microchim. Acta* **2020**, *187* (5), 1-10.
(48) Zhu, M.; Chen, P.; Liu, M. Sunlight-driven plasmonic photocatalysts based on Ag/AgCl nanostructures synthesized via an oil-in-water medium: enhanced catalytic performance by morphology selection. *J. Mater. Chem.* **2011**, *21* (41), 16413-16419.
(49) Kuzmenko, V.; Wang, N.; Haque, M.; Naboka, O.; Flygare, M.; Svensson, K.; Gatenholm, P.; Liu, J.; Enoksson, P. Cellulose-derived carbon nanofibers/graphene composite electrodes for powerful compact supercapacitors. *RSC adv.* **2017**, *7* (73), 45968-45977.
(50) Kresse, G.; Furthmüller, J. Efficiency of ab-initio total energy calculations for metals and semiconductors using a plane-wave basis set. *Comput. Mater. Sci.* **1996**, *6* (1), 15-50.
(51) Blöchl, P. E. Projector augmented-wave method. *Phys. Rev. B* **1994**, *50* (24), 17953.
(52) Perdew, J. P.; Burke, K.; Ernzerhof, M. Generalized gradient approximation made simple. *Phys. Rev. Lett.* **1996**, *77* (18), 3865.
(53) Monkhorst, H. J.; Pack, J. D. Special points for Brillouin-zone integrations. *Phys. Rev. B* **1976**, *13* (12), 5188.
(54) Grimme, S. Semiempirical GGA-type density functional constructed with a long-range dispersion correction. *J. Comput. Chem.* **2006**, *27* (15), 1787-1799.
(55) Tripathi, A.; Hareesh, C.; Sinthika, S.; Andersson, G.; Thapa, R. CO oxidation on Pt based binary and ternary alloy nanocatalysts: Reaction pathways and electronic descriptor. *Appl. Surf. Sci.* **2020**, *528*, 146964.
(56) Yao, G.; Zhai, Z.; Zhong, J.; Huang, Q., DFT and SERS study of 15N full-labeled adenine adsorption on silver and gold surfaces. *J. Phys. Chem. C* **2017**, *121* (18), 9869-9878.
(57) Yao, G.; Huang, Q., DFT and SERS Study of l-Cysteine Adsorption on the Surface of Gold Nanoparticles. *J. Phys. Chem. C* **2018**, *122* (27), 15241-15251.
(58) Kumar, D.; Jain, V.; Rai, B., Unravelling the mechanisms of corrosion inhibition of iron by henna extract: A density functional theory study. *Corros. Sci.* **2018**, *142*, 102-109.

(59) Pereira, A. F. d. F.; de Souza Junior, E.; Ghosh, A., Structural stability and electronic characteristics of cellulose nanowires on graphene-like systems. *Appl. Surf. Sci.* **2021**, *569*, 150998.

(60) Ebrahimi, J.; Ahangari, M. G.; Jahanshahi, M., Computational studies at the density functional theory (DFT) level about the surface functionalization of hexagonal monolayers by chitosan monomer. *Appl. Surf. Sci.* **2018**, *440*, 778-789.

(61) Zhou, Z.; Bai, X.; Li, P.; Wang, C.; Guo, M.; Zhang, Y.; Ding, P.; Chen, S.; Wu, Y.; Wang, Q., Silver nanocubes monolayers as a SERS substrate for quantitative analysis. *Chin. Chem. Lett.* **2021**, *32* (4), 1497-1501.

(62) Montaño-Priede, J. L.; Pal, U., Estimating near electric field of polyhedral gold nanoparticles for plasmon-enhanced spectroscopies. *J. Phys. Chem. C* **2019**, *123* (18), 11833-11839.

(63) Johnson, P. B.; Christy, R.-W., Optical constants of the noble metals. *Phys. Rev. B* **1972**, *6* (12), 4370.

(64) Merk, V.; Nerz, A.; Fredrich, S.; Gernert, U.; Selve, S.; Kneipp, J., Optical properties of silver nanocube surfaces obtained by silane immobilization. *Nanospectroscopy* **2014**, *1*, 19-25.

TOC

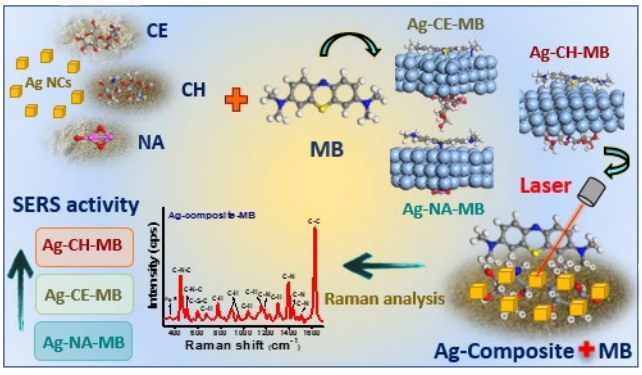

Nontechnical synopsis

The hazardous dye, methylene blue (MB) can be detected at ultra-low concentration using Ag-composites via surface enhanced Raman scattering (SERS).